








Geological and geophysical studies of the Agoudal impact structure (Central High Atlas, Morocco): New evidence for crater size and age

Houda EL KERNI ^{*}, Hasnaa CHENNAOUI AOU DJEHANE ¹, David BARATOUX ^{2,3},
Mohammed AOU DJEHANE⁴, André CHARRIÈRE⁵, Hassan IBOUH⁶, Pierre ROCHETTE ⁷,
Yoann QUESNEL⁷, Minoru UEHARA⁷, Thomas KENKMANN ⁸, Gerwin WULF⁸,
Michael POELCHAU ⁸, Van Binh NGUYEN⁹, Maria ABOULAHRISS ^{1,7}, Samira MAKHOUKHI¹,
Georges AUMAÎTRE⁷, Didier BOURLÈS⁷, and Karim KEDDADOUCHE⁷

¹Faculty of Sciences Ain Chock, GAIA Laboratory, Hassan II University of Casablanca, km 8 Route d'El Jadida, 20150 Casablanca, Morocco

²Géosciences-Environnement-Toulouse, Université Paul Sabatier CNRS & IRD UMR 5563, 14 Avenue Edouard Belin, 31 400 Toulouse, France

³Institut Fondamental d'Afrique Noire Cheikh Anta Diop, Dakar, Senegal

⁴152 Lotissement Nassim Islane, 20190 Casablanca, Morocco

⁵13 Terrasses de la Figuière, 30140 Anduze, France

⁶Geology Department, Faculty of Sciences and Techniques, Cadi Ayad University of Marrakesh, Marrakesh, Morocco

⁷Aix-Marseille University, CNRS, IRD, INRA, Coll France, CEREGE, Aix-en-Provence, France

⁸Institute of Earth and Environmental Sciences, Geology Albert-Ludwigs-University Freiburg, Albertstrasse 23-b, 79104 Freiburg, Germany

⁹Faculty of Environment, Hanoi University of Mining and Geology, 11910, North Tu Liem District, Ha Noi, Vietnam

*Corresponding author. E-mail: houdaelkerni@gmail.com

(Received 03 August 2018; revision accepted 30 May 2019)

Abstract—Since the discovery of shatter cones (SCs) near the village of Agoudal (Morocco, Central High Atlas Mountains) in 2013, the absence of one or several associated circular structures led to speculation about the age of the impact event, the number, and the size of the impact crater or craters. Additional constraints on the crater size, age, and erosion rates are obtained here from geological, structural, and geophysical mapping and from cosmogenic nuclide data. Our geological maps of the Agoudal impact site at the scales of 1:30,000 (6 km²) and 1:15,000 (2.25 km²) include all known occurrences of SCs in target rocks, breccias, and vertical to overturned strata. Considering that strata surrounding the impact site are subhorizontal, we argue that disturbed strata are related to the impact event. Three types of breccias have been observed. Two of them (br1-2 and br2) could be produced by erosion–sedimentation–consolidation processes, with no evidence for impact breccias, while breccia (br1) might be impact related. The most probable center of the structure is estimated at 31°59'13.73"N, 5°30'55.14"W using the concentric deviation method applied to the orientation of strata over the disturbed area. Despite the absence of a morphological expression, the ground magnetic and electromagnetic surveys reveal anomalies spatially associated with disturbed strata and SC occurrences. The geophysical data, the structural observations, and the area of occurrence of SCs in target rocks are all consistent with an original size of 1.4–4.2 km in diameter. Cosmogenic nuclide data (³⁶Cl) constrain the local erosion rates between 220 ± 22 m Ma⁻¹ and 430 ± 43 m Ma⁻¹. These erosion rates may remove the topographic expression of such a crater and its ejecta in a time period of about 0.3–1.9 Ma. This age is older than the Agoudal iron meteorite age (105 ± 40 kyr). This new age constraint excludes the possibility of a genetic relationship between the Agoudal iron meteorite fall and the formation of the Agoudal impact site. A chronology chart including the Atlas orogeny, the alternation of sedimentation and erosion periods, and the meteoritic impacts is presented based on all obtained and combined data.

INTRODUCTION

Agoudal is the only known impact structure in Morocco (Chennaoui Aoudjehane et al. 2016). It was confirmed by the observation of well-preserved shatter cones (SCs) in a mid-Jurassic marly limestone formation (Sadilenko et al. 2013; Chennaoui Aoudjehane et al. 2014; El Kerni et al. 2014; Lorenz et al. 2015). SCs have only been reported unambiguously for structures larger than 1 km in diameter and occur typically within 1/6–1/2 of the estimated radius of an impact structure (Baratoux and Reimold 2016). Field work and satellite image analysis did not reveal any circular structure associated with the SC occurrences. Vertical to overturned N150–N160 trending strata, not observed elsewhere in the surrounding area, were reported by Chennaoui Aoudjehane et al. (2016). The breccias within the area of SC occurrence were considered to be impact breccias, based on the presence of cryptocrystalline inclusions, and were interpreted as possible relics of weathered impact melt rocks (Lorenz et al. 2015). These breccias may have been alternatively formed as a result of erosion, weathering, and cementation processes (Chennaoui Aoudjehane et al. 2016). Erosion of the Agoudal impact structure may have wiped out the circular morphological expression of the crater. Considering regional denudation rates of $\sim 80 \text{ m Ma}^{-1}$ for the High Atlas Mountains (Ruiz et al. 2011), SC-bearing outcrops of $\sim 500 \times 300 \text{ m}$ in Agoudal, and the fact that the area of SC occurrence is commensurable with the size of the crater, Chennaoui Aoudjehane et al. (2016) proposed an age of the Agoudal impact event older than 1 Ma with a size of 1–3 km in diameter.

The area of SC occurrence overlaps with the strewn field of the Agoudal iron meteorite (Chennaoui Aoudjehane et al. 2013). Micrometric fragments of Schreibersite (a phosphide very rare on Earth but common in iron meteorites) were reported to be found on a SC surface by Schmieder et al. (2015). These observations led to a debate regarding a possible genetic link between the Agoudal iron meteorite and SC occurrence. This hypothesis was promptly disputed (El Kerni et al. 2014) and rejected by Chennaoui Aoudjehane et al. (2016), based on the incompatible age calculated for the Agoudal meteorite fall (Hutzler et al. 2014; Hutzler 2015) and the period of time required to remove the topographic expression of a crater larger than 1 km in diameter.

Lorenz et al. (2015) proposed a calculation model of several small craters genetically related to the Agoudal impact meteorite fall. The model has numerous problems, including the fact that SCs are not observed in association with such small impact craters.

This hypothesis was not confirmed by Chennaoui Aoudjehane et al. (2016).

In order to better constrain the size of the eroded crater and the age of the impact event, we collected new geological, structural, and geophysical observations. Detailed geological and structural maps were assembled. The concentric deviation method (Poelchau and Kenkmann 2008) was used to define the most probable center of the impact structure. The conducted geophysical survey of Agoudal combines ground magnetic field mapping and electromagnetic campaigns. We also measured the magnetic susceptibility of core samples to support the interpretation of the magnetic survey. Rather than relying on regional erosion rates (80 m Ma^{-1} ; Ruiz et al. 2011; Chennaoui Aoudjehane et al. 2016), we have constrained the local erosion rates from cosmogenic nuclide data based on two samples collected at the surface, within the area of SCs and outside of it, some 5 km SE of the disturbed area. These data are combined and analyzed together to infer more precise and robust conclusions regarding the age, position, and size of the impact structure. We have then established a chronology chart of terrestrial and extraterrestrial events at the Agoudal impact site, relying on the combined results data.

GEOLOGICAL CONTEXT OF THE AGOUDAL IMPACT STRUCTURE

The Agoudal impact structure lies in the Central High Atlas intracontinental mountain range (Morocco) (Fig. 1). The formation of this mountain range is related to the closure of the Neotethys (Laville et al. 1977). The mountain belt is predominantly built up of Jurassic rocks (Figs. 1–3). It has experienced extension and rifting. A first phase of extension occurred during the Triassic, as recorded by red beds (clays, silts, salt, and gypsum) and tholeiitic basalts. A later phase of extension occurred during the Jurassic, recorded by the deposition of marine carbonates and shales capped by continental red beds (Charrière and Haddoumi 2016). Sedimentation of transgressive lower Liassic platform carbonates, a continuous key stratigraphic level consisting of a few hundred meters of limestone and dolomite, sealed the Triassic rift basins (Laville et al. 1994; Piqué et al. 2000). During the late Liassic, the platform was drowned and disrupted (Brechtbuhler 1983; Warme 1988; Igmoullan 1993; Pesonen et al. 1998; Souhel et al. 2000). From Toarcian to Bajocian times (170–183 Ma), up to 5000 m of open marine shales (marls), calciturbidites, and reefal limestones accumulated in the central High Atlas. Red beds, indicating filling and regression, became widespread within the Bathonian strata (Choubert and Faure-Muret

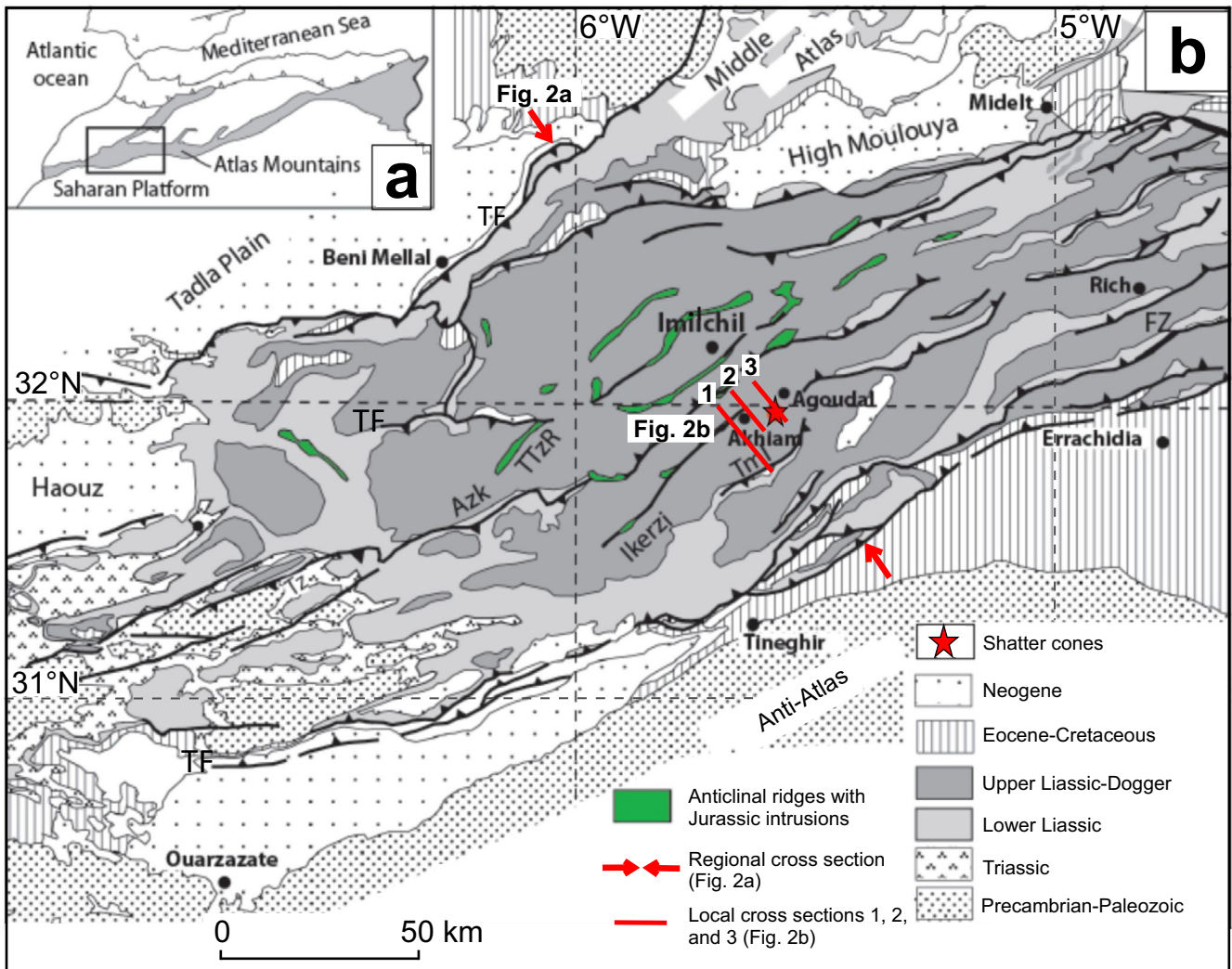


Fig. 1. a) Location of the Moroccan Central High Atlas. b) Schematic geology of the Central High Atlas region in Morocco with locations of the Agoudal village, the discovery site of shatter cones, the Akhlam valley in the High Atlas Mountains, anticlinal ridges, the synthetic regional cross section location, and the detailed local cross sections locations (TML = Tioumliline [Ridge]; FZ = Fom Zaabel; TTzR = Talmest-Tazoult Ridge; Azk = Azourki [Mountain]; Tz = Tizal [Mountain]; TF = Thrust Faults). Map modified after Teixell et al. (2003), Michard et al. (2011), and Chennaoui Aoudjehane et al. (2016). The regional cross section and the three local cross sections (2, 3, and 4) are presented in Figs. 2a and 2b, respectively. (Color figure can be viewed at wileyonlinelibrary.com.)

1962; Jenny et al. 1981). During this period, the Atlas troughs were characterized by a complex fault pattern, developed under a NW–SE tensional field. The Cretaceous strata are composed of basal red beds beneath a Cenomanian–Turonian limestone platform (Froitheim et al. 1988). The uppermost Cretaceous strata consist of terrigenous red beds, indicative of the onset of the Alpine compression (Laville et al. 1977; Froitheim et al. 1988; Amrhar 1995). Due to the successive shortening and erosion episodes, only minor remnants of the subaerial Upper Paleocene–Eocene deposits are preserved within the “gutters” of breached

ridges (Charrière et al. 2009; Michard et al. 2011) (Figs. 2 and 3).

The village of Agoudal lies above an altitude of 2000 m. It is located ~20 km to the southeast of the town of Imilchil (Fig. 1). Agoudal is surrounded in its northern and eastern parts by large synclines in lateral alternation with narrow anticlinal structures, commonly called “ridges,” with amplitudes ranging from several meters to hundreds of meters (Fig. 2a) (Michard et al. 2011; Ibouh and Chafiki 2017). The Agoudal impact structure is situated in the “flat-bottomed” zone, between Ikerzi and Toumliline ridges. These ridges are

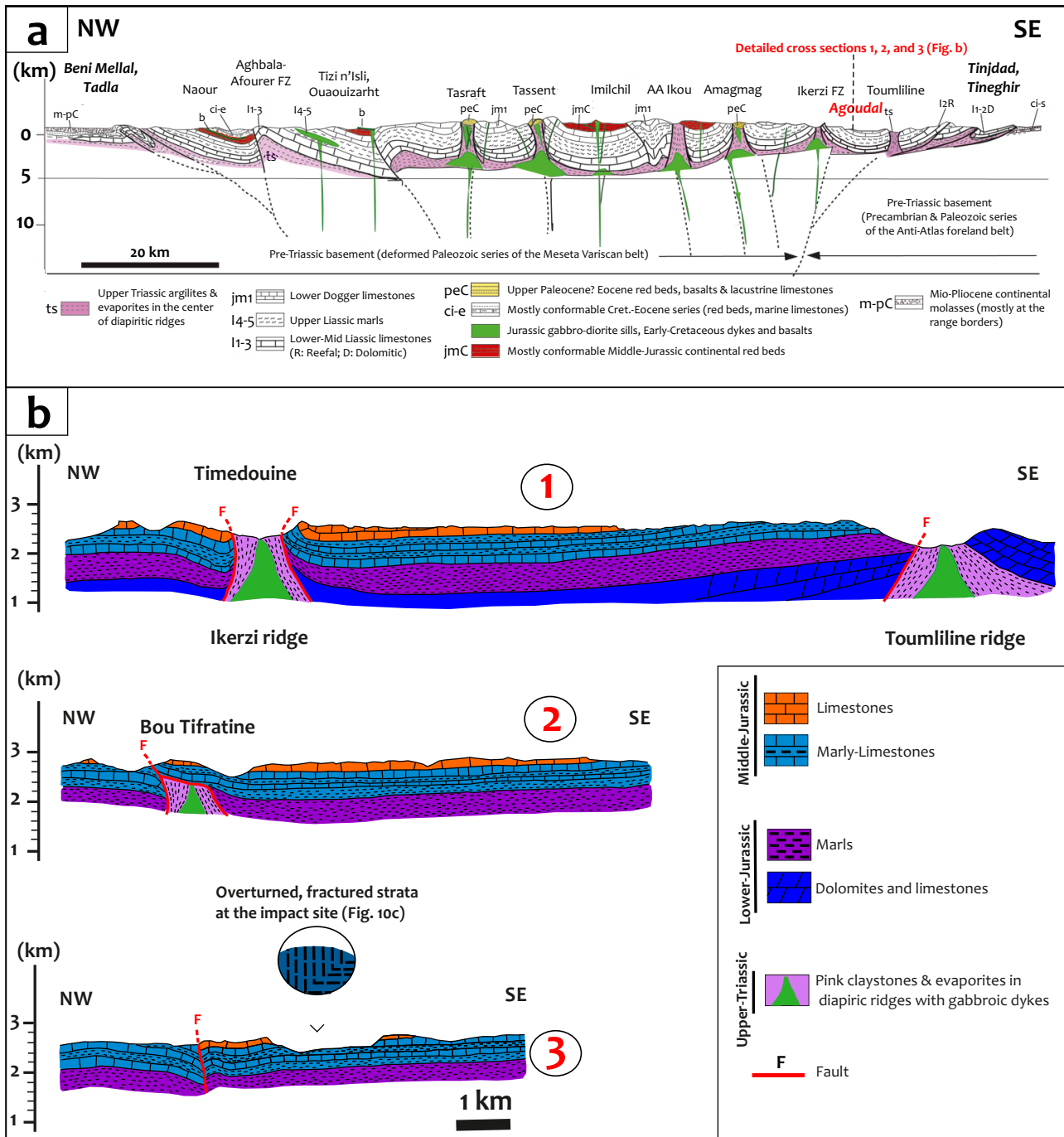


Fig. 2. a) Synthetic regional cross section cutting the Central High Atlas in NW-SE direction, and exposing anticlinal ridges with synclinal flanks. The Agoudal impact structure is situated between Ikerzi and Toumliline ridges in the central subhorizontal area. Modified after Michard et al. (2011) and Ibouh and Chafiki (2017). b) Detailed local cross sections 1, 2, and 3 in NW-SE direction, essentially exposing the subhorizontal part between the anticlinal ridges of Ikerzi and Toumliline, where the Agoudal impact structure is localized. The localization of the regional cross section (a) and the local cross sections (b) is in Fig. 1. (Color figure can be viewed at wileyonlinelibrary.com.)

mainly oriented N60 to EW. They are cored by Triassic basalts, Jurassic alkaline gabbro, and Liassic limestone. They expose a sedimentary series with marine limestone

deposits from the Liassic to the Bajocian–Bathonian (Figs. 2a and 2b). The Imilchil sedimentary series correspond to a regressive mega-sequence. These

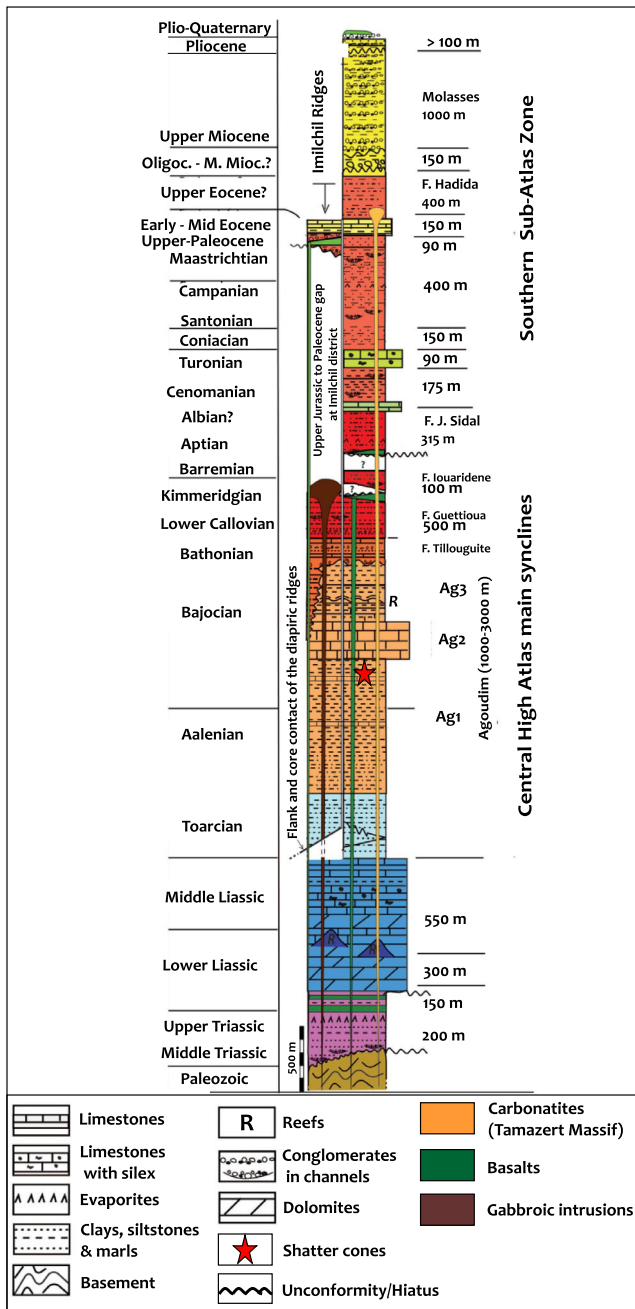


Fig. 3. Stratigraphic column of the Mesozoic–Cenozoic series of the Central High Atlas, modified after Ibouh and Chafiki (2017). (Color figure can be viewed at wileyonlinelibrary.com.)

anticlinal ridges were developed as “salt walls” during the Liassic–Middle Jurassic interval of time above dominant, NE-trending basement faults (Bouchouata et al. 1995; Ettaki et al. 2007; Michard et al. 2011; Ibouh et al. 2014). Preexisting diapirs have favored subsequent magma ascent, which played an important role in the genesis of the ridges (Bougadir 1991; Rahimi et al. 1991; Michard et al. 2011). The anticlinal ridges

correspond to upright folds, longitudinally curved (Figs. 2a and 2b), with dips ranging from 25 to 45° toward the north or the south (Ibouh 2004). They are alternated by large and “flat-bottomed” synclines (Ibouh 2004). The anticlinal fold system is associated with reverse faults that have been active during the Tertiary inversion (Frizon de Lamotte et al. 2008).

A Triassic salt diapir at Toumliline, located some 15 km SSW of the village of Agoudal, was formed during the Jurassic extension and was later deformed during the Alpine compression (Teixell et al. 2003) (Fig. 2a). The Agoudal stratigraphic series is related to the Tassent Formation (Ibouh 1995), considered to be the lower member of the Agoudim Formation by Studer and du Dresnay (1980). It is also named “Ag 1” by Charrière et al. (2011) (Fig. 3). It exhibits benthic macrofauna (bivalves, echinoderms, brachiopods, and corals) (Studer and du Dresnay 1980; Charrière et al. 2011) deposited during the Bajocian period (Middle Dogger, 170 Ma; Milhi 1997). Several layers of blue marl with reef limestones are exposed at the top of these hills (Fig. 2b). They overlie deposits of blue marl with brachiopods and oolitic limestone, which are exposed in the Akhiam valley (Chennaoui Aoudjehane et al. 2016).

MAGNETIC AND ELECTROMAGNETIC SIGNATURES OF SMALL (<10 KM) IMPACT CRATERS

Exposed impact structures are commonly associated with circular topographic signatures (depression, rim, ring, or peak) and tectonic features (concentric faults, tilted blocks, upturned, and/or uplifted strata) (Kenkmann et al. 2014). They are identified and confirmed by the presence of diagnostic criteria observed in the field at the mesoscale (SCs, see Baratoux and Reimold 2016) and/or in the laboratory at the microscopic scale (e.g., shocked quartz with planar deformation features; French and Koeberl 2010). They are also generally associated with geophysical signatures (which are not diagnostic of meteoritic impact) such as circular gravity, magnetic, electric conductivity, or radiometric anomalies (Pilkington and Grieve 1992; Boamah and Koeberl 2002; Vasconcelos et al. 2012; Baratoux et al. 2019). Geophysical analyses are also useful to explore for possible buried impact structures, which are then confirmed by the documentation of shock effects from samples obtained from drill cores (e.g., Kenkmann et al. 2015). Geophysical signatures of eroded or buried impact structures are often preserved (Pilkington and Grieve 1992) and provide insights about their initial dimensions. When an impact

structure is partially exposed, the geophysical studies are conducted together with detailed structural and geological mapping, including mapping of shocked material (Ormö et al. 1999). Geophysical studies are also usually achieved before drilling an impact structure in order to optimize the scientific output of drilling, as in the case of the Bosumtwi impact structure (Koeberl et al. 2007).

In the case of the Agoudal impact site, the choice of applicable geophysical investigations is limited. The relief is a challenge for the interpretation of gravimetric data. The rocky surface hampers the application of electric methods due to poor electrode implantation. Ground magnetic field and electromagnetic methods (measurement of subsurface conductivity based on electromagnetic induction) are appropriate in these conditions and were applied to an area encompassing the domain of occurrence of SCs. Given the range of probable diameters of the impact crater that was formed at Agoudal (1–3 km; Chennaoui Aoudjehane et al. 2016), we review here the magnetic and conductivity signatures of small (<10 km) impact structures.

Generally, the magnetic signature of a small impact structure is a circular low, ranging in amplitude from tens to a few hundred nanoTeslas (nT) (Clark 1983). A broad correlation exists between the extent of the anomaly and the crater size. All structures with $D < 10$ km have magnetic lows, which are best defined over simple craters, for example, Barringer Crater (1.2 km), USA; West Hawke Lake crater (2.44 km), Canada; and Wolfe Creek Crater (0.88 km), Australia (Fudali 1979; O'Neill and Heine 2005). Three impact structures in Finland, Karikkoselkä, Paasselkä, and Suvasvesi South also show such magnetic anomaly lows (Pesonen et al. 1992, 1998; Salminen 2011). The fractured target rocks show reduced magnetization levels, suggesting that the propagating shock wave is the likely cause of this signature.

Electromagnetic methods have been infrequently applied in impact structure analysis. The conductivity of rocks strongly depends on their water content. The degree of fragmentation influences the porosity, the amount, and the distribution of fluids within the rock, and hence reduces its conductivity (Pilkington and Grieve 1992). However, sealed fractures may increase the bulk-rock resistivity. For example, at Siljan (Sweden), Henkel (1992) noted an increase in resistivity coinciding with the central uplift. This technique has also been applied to thickness mapping of crater fill breccias and postimpact sedimentary fill, identified by a low resistivity response due to high porosity and permeability of these layers (e.g., Araguinha, Brazil; Tong et al. 2010).

METHODS

Geological Mapping

The results from several field campaigns are assembled and presented in a new geological map at a scale of 1:30,000. More than 1000 measurements of strike and dip directions of strata, faults, and joints were taken over an area of $\sim 3000 \times 2000$ m surrounding and including the SC outcrops. The extent of the area was determined as a compromise between the need for detailed observations in the SC area and its immediate vicinity, the available time, and resources for field work. Furthermore, observations from satellite images as well as regional and local geological settings (Figs. 2a and 2b) do not suggest that critical deformation of layers in relation to the impact structure is expected to be found beyond this area. The map was drawn using CorelDraw-6 software. The exposure of rocks is fairly good, due to the absence of vegetation.

A second geological map at a scale of 1:15,000 was made of the central area (1500×1500 m, 2.25 km^2) including the SC outcrops, the breccias, and vertical to overturned strata. This focused mapping effort at higher resolution is justified given the lack of signs of disturbance related to the impact event outside of this area, and the importance of reporting the localization and extension of outcrops within the disturbed area, as well as the information that they might provide on the original shape of the impact crater.

Structural Methods

A third map, based on a previously published structural map (Chennaoui Aoudjehane et al. 2016), includes structural observations of faults and joints along with the SC sample locations (Fig. 4). The structural measurements were spatially interpolated using the natural neighbor interpolation technique. This method produces a continuous map of dip angles and dip azimuths (see, Kenkmann et al. [2017] for more detail about the technique).

We also applied the technique of concentric deviation to these observations, which quantifies the deviations of observed strike from concentric strike for a given center. It consists in the conversion of structural data into polar coordinates (distance to center, azimuth) followed by the analysis of the asymmetry of structural data in this coordinate system (Poelchau and Kenkmann 2008). The technique reveals, for instance, the structural asymmetries of impact craters (Poelchau and Kenkmann 2008). In our case, this technique is used in order to estimate the likelihood of the location of the center of the impact structure, based on the

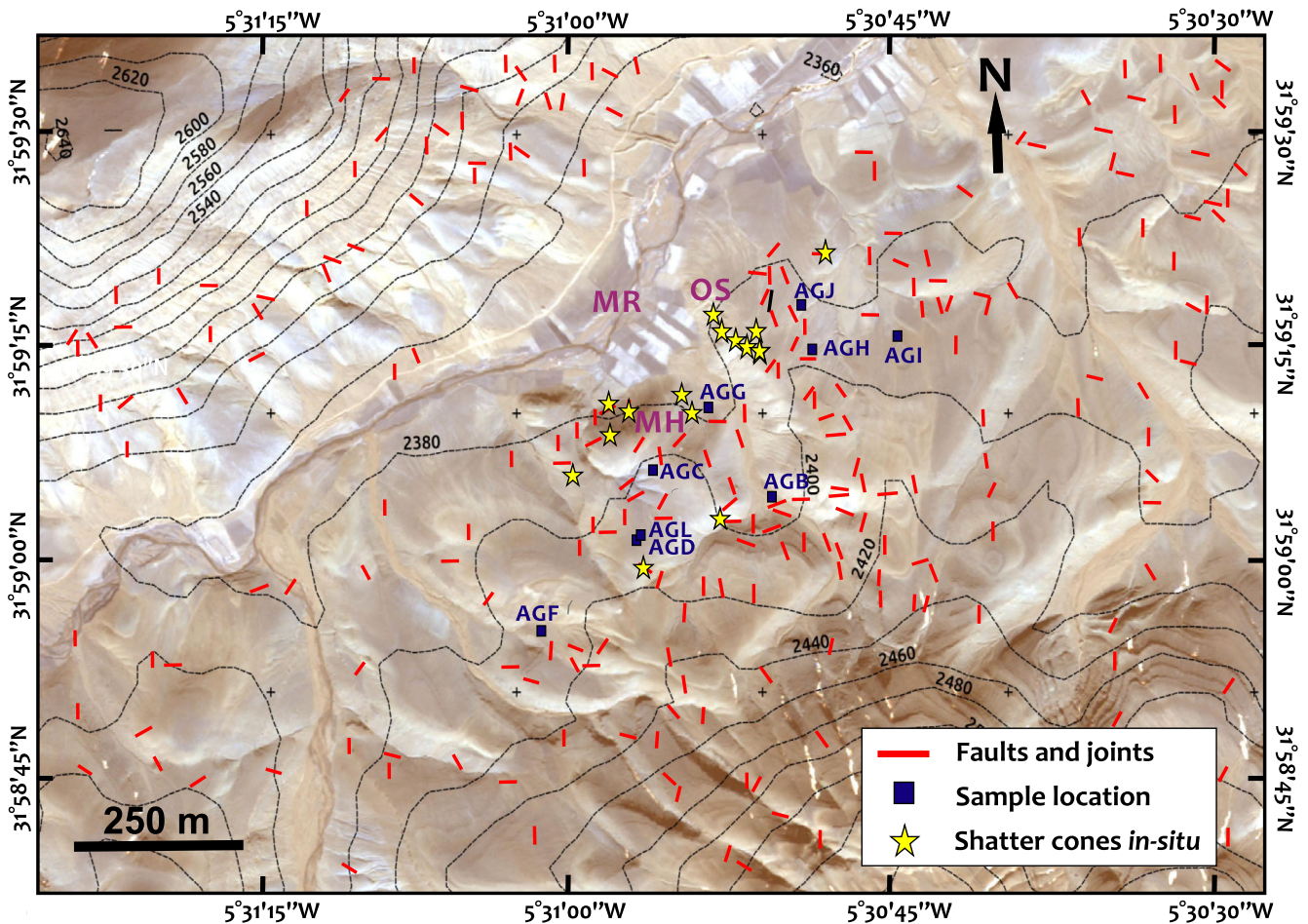


Fig. 4. Fault and joint system, and sample locations, plotted on a topographic map of the Agoudal impact structure (Central High Atlas, Imilchil district-Morocco) superimposed on a WorldView-2 Satellite image. Samples taken for magnetic properties and cosmogenic measurements are named from AGA to AGM (AG stands for Agoudal). AGA, AGE, AGK, and AGM samples taken 5 km SE of the studied area are not shown on the map. “OS,” “MR,” and “MH” refer to vertical to “overturned strata,” “Main River,” and “Main Hill,” respectively. (Color figure can be viewed at wileyonlinelibrary.com.)

available dip and azimuth data of the strata. Axial symmetry should be highest when the center of the polar coordinate system corresponds to the center of the impact structure.

We have converted 350 measurements of strike and dip directions of the strata along with latitude and longitude values taken over the central disturbed area of $\sim 1500 \times 1500$ m from a geographic reference system into polar coordinates. The accuracy of GPS measurements is about 1 m. Eight potential centers, distributed over the mapped area, and including positions near the main SC area or near the river, were tested with the concentric deviation method. The latitudes and longitudes of the measurement points and the presumed chosen crater center were given as inputs. In some cases, plots display scattering. To get a better overview of possible average deviations, plots require

smoothing. The “overlapping bins” method is the preferred method of smoothing. All data within a defined sector are averaged. A bin size of 30° is used by default and the position of this bin is varied in steps of 10° . All values within a 30° range from 345° to 15° are collected, starting directly at azimuth = 0° . The arithmetical average is calculated and displayed for 0° . The next value is calculated for all data between 355° and 25° , for a step size of 10° , and displayed at 10° , then from 5° to 35° for 20° , etc., yielding 36 points of average concentric deviation. A strike that is tangential to a hypothetical circle around the crater center is defined as “concentric” and has a concentric deviation value of 0° . A strike that is rotated clockwise relative to the tangent to the hypothetical circle has a positive concentric deviation value, while a counterclockwise rotation is noted with a negative value. Strike is

displayed with an exaggeration factor of $2\times$, which is the minimal value that enhances the visualization of the nonconcentric behavior.

Electromagnetic Data Acquisition

A Geonics EM 34-3 ground conductivity meter and a 20-m coil separation were used for all electromagnetic measurements. The reader is referred to Jones et al. (1992) for a detailed description of the method of acquisition of ground subsurface conductivity and instrument characteristics. The typical exploration depths are 15 and 30 m in the horizontal and vertical dipole configuration, respectively (McNeill 1980). Another profile was measured using a 10-m coil separation to observe the shallower conductivity distribution. For each point, coordinate measurements were taken by a GPS device.

Magnetic Measurements

Magnetic Field Mapping

The ground magnetic field data were collected along several profiles using a Geometrics cesium vapor magnetometer (G-858). Considering human walking speed and topography, combined to a 1-min sampling rate, the mean spatial separation between two consecutive measurements is about 10–15 m. The line spacing is about 100 m. The area of acquisition of 1 km^2 is centered around the SCs. The data were corrected for diurnal, and more generally, for external field variations, using the combination of our own measurements and data from surrounding INTERMAGNET observatories (Thébault et al. 2015). These fixed data also gave us a regional reference value for the Earth's magnetic field (due to the core dynamo and the crustal rock magnetization), which is close to the IGRF (International Geomagnetic Reference Field) predicted field value for the survey period (May 2014) and location. This value was subtracted from the data previously corrected for external field variations to resolve the anomaly. Then, an interpolated grid of the magnetic anomaly values was built using a nearest-neighbor method (Thébault et al. 2015) and projected upward to a single altitude of 2600 m. Lastly, a standard reduction-to-the-pole (RTP) procedure was applied to center the anomalies above magnetized sources (Blakely 1995).

Magnetic Properties of Rock Samples

We sampled 88 core samples (2.2 cm long and 2.5 cm diameter) at 12 sites, from different lithologies and from inside and outside the disturbed zone, using a gas-powered drill. They were named from AGA to

AGM. AGE, AGM, AGK, and AGA samples were taken 5 km SE of the studied area (not shown on the maps) to make sure that these samples were not affected by the impact (Fig. 4). The majority of the cores were drilled in Bajocian limestone sites; other cores consist of breccias and of Quaternary alluvium. Magnetic susceptibility (K) was measured using a MFK1 Kappabridge and natural remnant magnetization (NRM) using a 2G DC Squid magnetometer. These parameters were used to estimate in situ total magnetization using a total present-day field (PDF) of $41\text{ }\mu\text{T}$ (which is the average value of magnetic field intensity in the Agoudal area at the time of acquisition). Magnetic mineralogy was also evaluated using hysteresis measurements with a Micromag VSM (one Tesla maximum field).

Cosmogenic Nuclides

Two limestone samples were collected at the surface, one near the main SC outcrop (AGG) (Fig. 4), and one outside of the disturbed zone, 5 km SE of the studied area (AGE). Samples were crushed, sieved, and Cl was chemically extracted as AgCl. Cl and ^{36}Cl concentrations were then determined by isotope dilution accelerator mass spectrometry from the measured $^{35}\text{Cl}/^{37}\text{Cl}$ and $^{36}\text{Cl}/^{35}\text{Cl}$ ratio. These measurements were performed at the French national Aix-Marseille Université facility Accélérateur pour les Sciences de la Terre, Environnement, Risques (Centre Européen de Recherche et d'Enseignement des Géosciences de l'Environnement, Aix-en-Provence). The ^{36}Cl and Cl concentrations were normalized to a ^{36}Cl standard prepared by Nishiizumi et al. (2017), which is KNSTD1600 with a given $^{36}\text{Cl}/^{35}\text{Cl}$ value of $(2.11 \pm 0.06) \times 10^{-12}$ (Fifield et al. 1990; Sharma et al. 1990). The decay constant of $2.303 \pm 0.016 \times 10^{-6}\text{ yr}^{-1}$ used corresponds to a ^{36}Cl half-life ($t_{1/2}$) of $3.014 \times 10^5\text{ yr}$. Analytical uncertainties include counting statistics, machine stability, and blank correction. As the age of the formation of the Atlas orogeny is older than 0.5 Ma, the two samples can be interpreted as being at a steady state in terms of cosmogenic nuclide production, and the ^{36}Cl concentration can then be quantitatively interpreted as a denudation rate (Biermann and Steig 1996; Schimmelpfennig et al. 2009).

RESULTS

Geomorphology and Lithology

The central area of the crater structure is dominated by Jurassic (Aalenian–Lower Bajocian age) marly limestone (Figs. 2a and 2b). This formation is

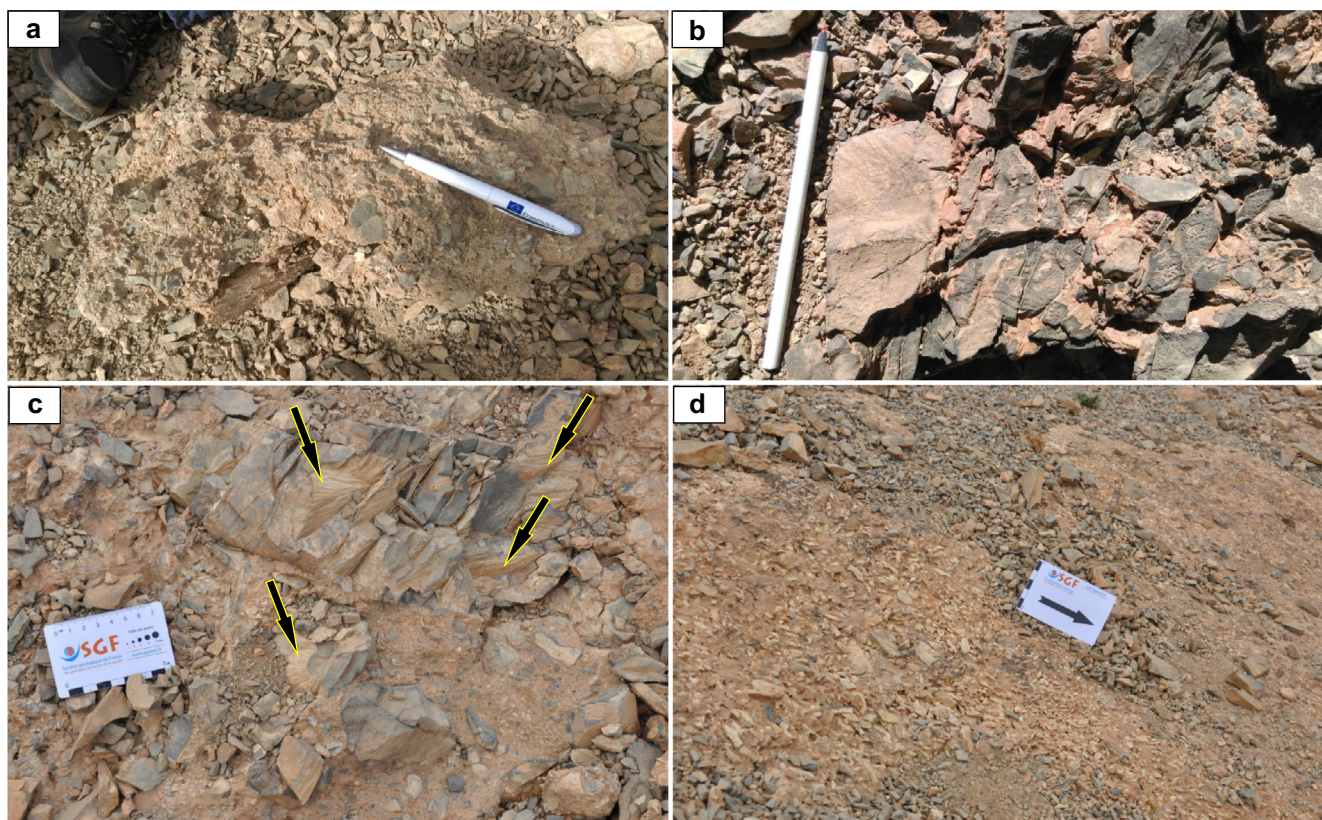


Fig. 5. Field photos of coarse-grained breccia (br1) and fine-grained breccia (br2) breccia deposits; (a) br1, (b) br1 filling the fractures of the highly fractured limestone formation in the shatter cone area, (c) br1 with large pieces of shatter cones (SCs are marked with arrows), and (d) br2 interpreted as a cemented scree slope. Pen for scale is 10 cm long. (Color figure can be viewed at wileyonlinelibrary.com.)

folded and fractured. Some fractures are filled by calcite; others are filled by fault gouge. Offset between faults walls are observed. The dip direction of the faults planes is mostly of N20°. Limestone formations are intercalated with brittle marl layers of variable thickness (up to 6 m). The dark color of marl is due to the weathering and a high content of organic matter. At the northeastern part of the impact site (Fig. 4), and in particular down the cliff, black scree slopes are abundant. They mostly fill the thalwegs at the bottom of the cliff. Quaternary alluvial deposits of the Rharbian (0.006 Ma; for more details about this formation, see Beaudet et al. 1967) cover the majority of the Jurassic formations. They are located especially in the southern part of the studied area, on the top of the “Main Hill” with the main outcrops of SCs. Reddish silts of Sultanian age (0.01–0.1 Ma; Beaudet et al. 1967) are relatively thick, especially in the thalwegs. The valleys are filled with rounded pebbles and bioclastic limestone fragments of sedimentary origin.

Shatter cones occur in a dark gray marl to marly limestone of the Agoudim Formation of Aalenian to

Lower Bajocian age (Studer and du Dresnay 1980), also described as the Agoudim 1 Formation “Ag 1” (Fig. 3) (Charrière et al. 2011). They are well developed, with curved surfaces of various orientations and diverging striations and meet all the criteria listed by Baratoux and Reimold (2016). New outcrops of marly limestone with SCs were discovered during the 2018 field campaign with respect to the earlier map of SC occurrences (Chennaoui Aoudjehane et al. 2016). The outcrops with SCs, including these new findings, define an area of occurrence of 700 × 400 m. Floating SCs are scattered over an area of ~900 × 700 m.

Three populations of breccias were observed and mapped (Fig. 5), “br1,” “br2,” and “br1-2.” They were exclusively observed near the area of SC occurrences and near the vertical to overturned strata locations.

The “br1” breccia is a calcareous coarse-grained consolidated breccia, with two populations of carbonate material: the breccia matrix between the marl/shale fragments and carbonate clasts (Figs. 5a and 5b). In some cases, this breccia fills the fractured limestone formations (Fig. 5b) and includes SC fragments in other locations (Fig. 5c). The matrix is abundant (more than

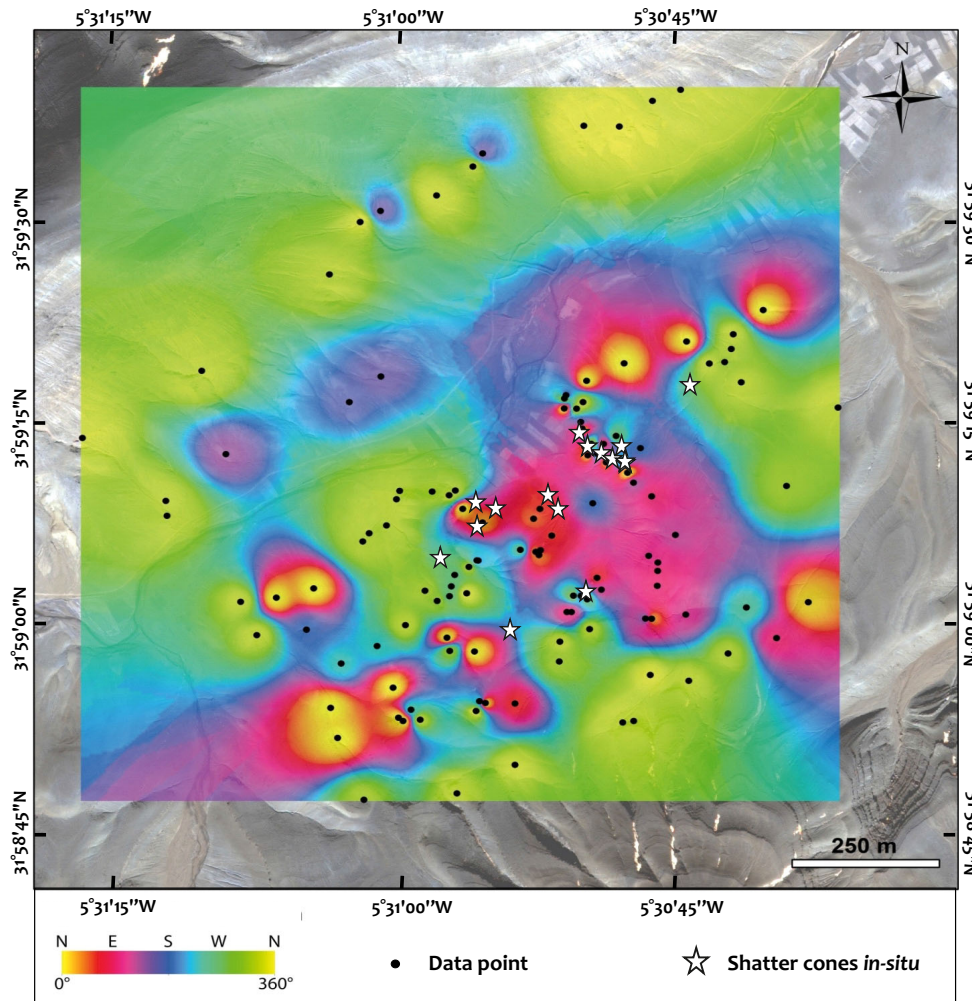


Fig. 6. Interpolated dip angles of strata measured over the Agoudal impact site and superimposed on a WorldView-2 satellite image. Interpolation is done by natural neighbor interpolation technique using 10 neighboring data. (Color figure can be viewed at wileyonlinelibrary.com.)

50% in volume) and has a light beige color. Clasts are angular and poorly sorted. The breccia deposit has a thickness of 0.2–0.3 m. A total of four thin sections of “br1” from four samples collected at the same location were studied under the optical microscope. Almost all clasts have a micritic texture without fossils. The matrix is a clean sparry calcite.

The “br2” breccia is a fine-grained breccia and represents a pinkish calcareous duricrust with angular fragments of marly Jurassic limestone (Fig. 5d). Cathodoluminescence analysis of several Agoudal breccia samples has shown one generation of clasts (Chennaoui Aoudjehane et al. 2016). The thickness of the deposit ranges from 0.3 to 0.5 m. These fragments are well sorted and appear to show a preferred orientation parallel to the slope. This breccia is

interpreted as a cemented scree slope. Similar noncemented scree slopes are observed in the disturbed area with fragments of similar dimensions.

The “br1-2” is a poorly sorted medium-grained marly Jurassic limestone breccia. The particle size ranges from 0.01 to 0.1 m. It represents an intermediate facies between “br1” and “br2.” This breccia deposit has an average thickness between 0.3 and 0.5 m. It contains more matrix than “br1,” but less than “br2.” The matrix is more altered and more whitish than in “br1” and “br2” breccias, probably due to a prolonged alteration by stagnant water under the red silts on a fairly flat topography. The three populations of breccia are exclusively observed near the area of SC occurrences and the vertical to overturned strata location.

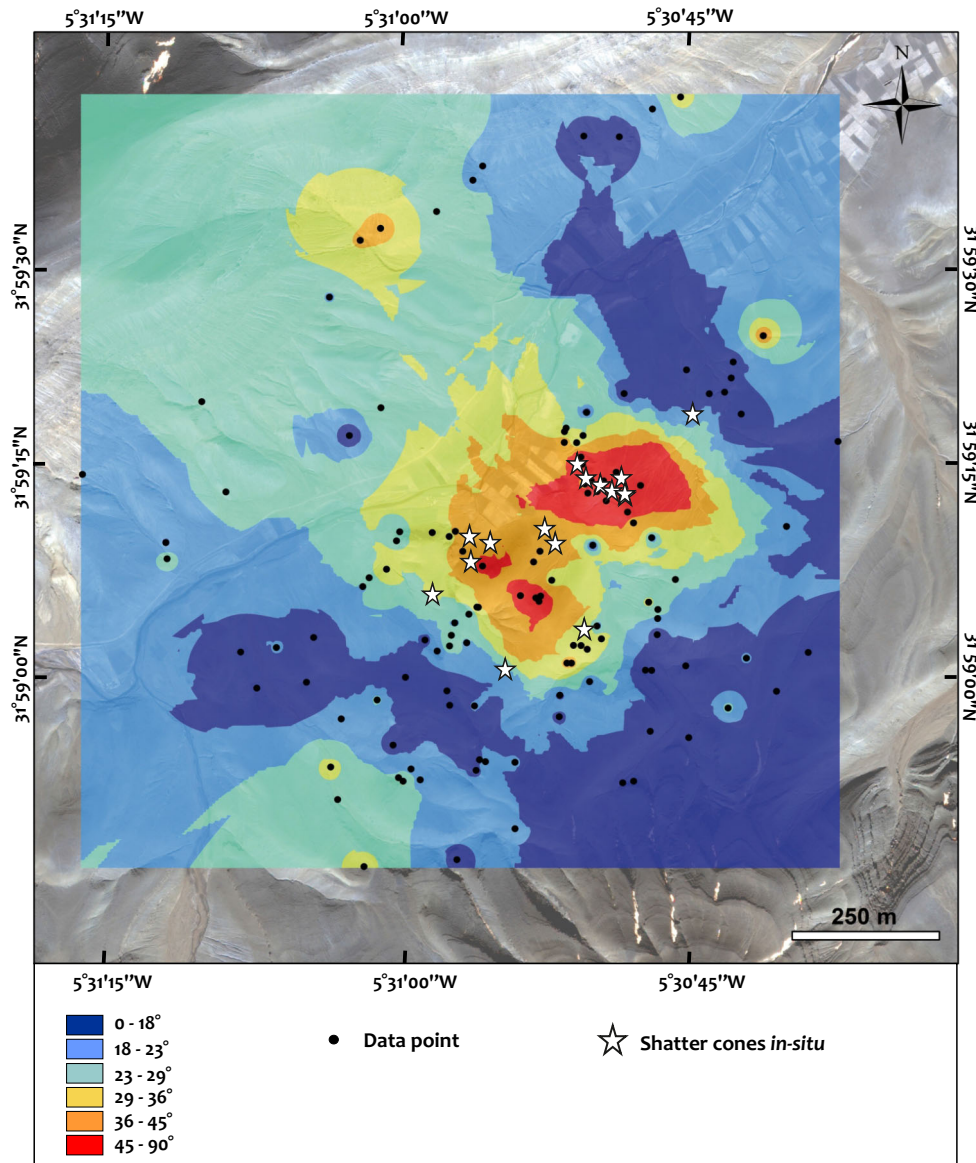


Fig. 7. Interpolated dip azimuths of strata measured over the Agoudal impact site and superimposed on a WorldView-2 satellite image. Interpolation is done by natural neighbor interpolation technique using 10 neighboring data. (Color figure can be viewed at wileyonlinelibrary.com.)

Analysis of Structural Measurements

The spatial distribution of faults and joints is given in Fig. 4. The disturbed area with SC outcrops, breccias, and the vertical to overturned strata is surrounded by subtabular formations. The subtabular formations surrounding the disturbed area along the NE–SW profile are fractured and mostly intercalated by marls of up to 50 cm with a strike parallel to the most common trend in the Atlas, N70°. The subtabular formations consist of the thickest limestone units within the Bajocian series, reaching up to 20 m thickness. The

fractured limestone formations are mostly affected by faults and joints related to the Atlas orogenic shortening with no obvious structural features that could be related to the impact event (Ibouh 1995; Chennaoui Aoudjehane et al. 2016). The fractures are filled with narrow to centimeter-sized calcite veins. Faults striking along N–S and E–W directions are steeply dipping. They are most likely related to the High Atlas regional tectonics.

The map of dip angles, covering the central area of 2.25 km² (Fig. 6), shows a disturbed area with a diameter of 0.12 km² (in red), with two

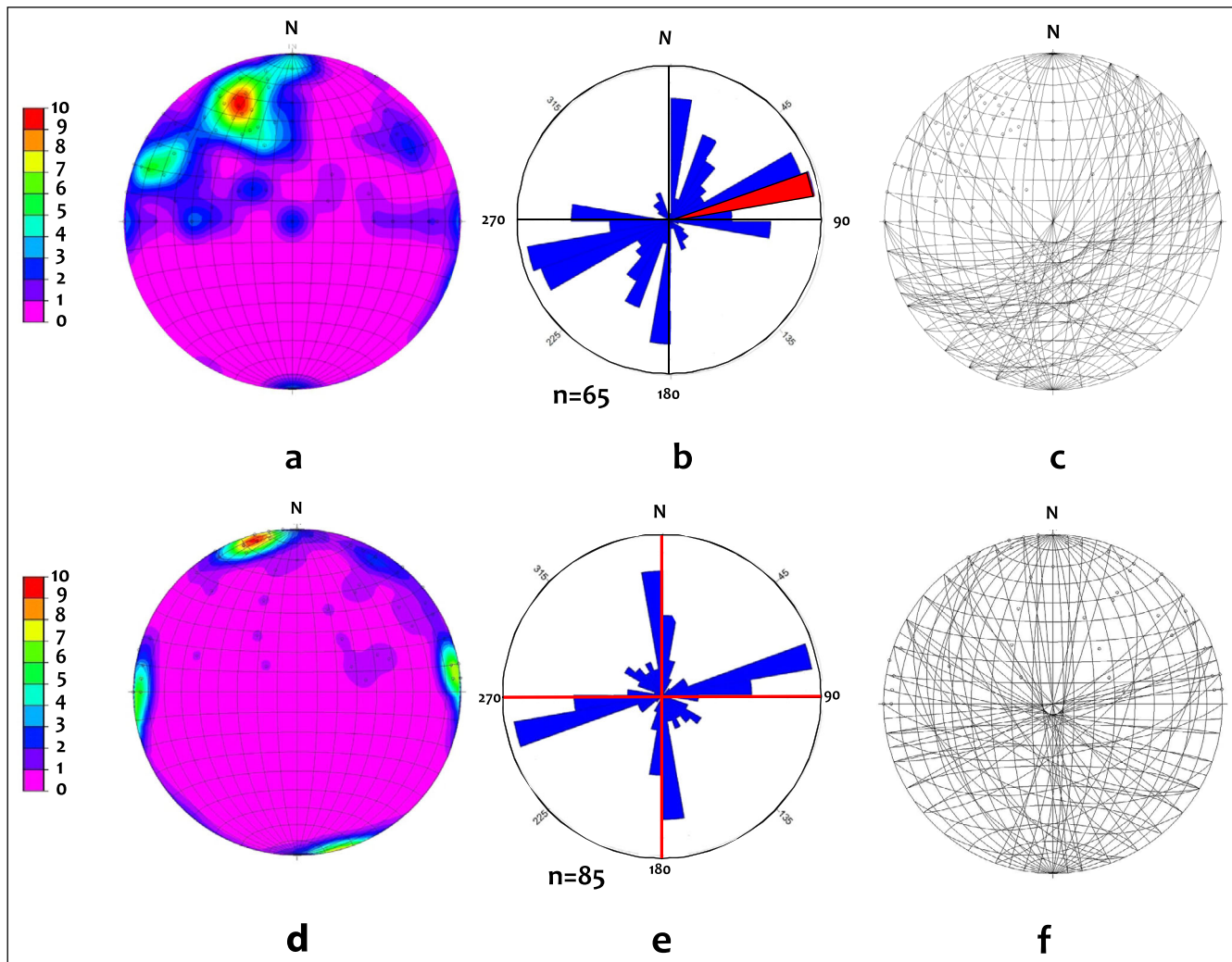


Fig. 8. Top: orientation data of bedding planes in the Agoudal area ($n = 65$). a) Density distribution of surface poles (color scale in %), (b) rose diagram of bedding strike with the trace of the most common strike in the High Atlas (N70°) marked in red, (c) stereogram of bedding planes (lines) and surface poles (dots). This series of plots shows how bedding orientation is different from the High Atlas trend. This local disturbance is most likely due to the impact event. Bottom: orientation data of faults and joints (fracturing in general) ($n = 85$). d) Density distribution of fracture surface poles. e) Rose diagram of the strike of the fault and fracture planes with the most common tectonic fracture directions related to the Atlas orogenic shortening, N-S and E-W, marked in red. f) Stereogram showing the orientation of fault and fracture planes (lines) and the poles of these planes (dots). The bottom series of plots shows that the fracturing in the studied area is similar to the fracturing recognized in the High Atlas. All measurements were taken over the mapped area of 6 km², including the area with SC outcrops. (Color figure can be viewed at wileyonlinelibrary.com.)

domains with enhanced dipping (vertical to overturned strata), which correspond to the SC outcrops. The vertical and overturned strata show either a WNW–ESE or a NE–SW trend (Chennaoui Aoudjehane et al. 2016). It should be mentioned that another vertical layer, with a N–S direction, was observed at the “Main Hill” (MH, Fig. 4). The “Main Hill,” with SC outcrops, is surrounded by subhorizontal beds with the most common trend in the Atlas, N70°. Our data show that the vertical to overturned layers are not related to the Atlas

deformation. Dip azimuths ranging from 50° to 230°, appearing in red on the dip azimuth map of the strata (Fig. 7), seem to be correlated with the SC area. The chaotic mixture of limestone, marl, and red soil with locally tabular or irregular breccia deposits precludes clear distinction of structural features or stratification at the “Main Hill” (Chennaoui Aoudjehane et al. 2016). Note that interpolation results in the agricultural fields “AF” being unreliable since no measurement of strike or dip was done in this area (absence of outcrops).

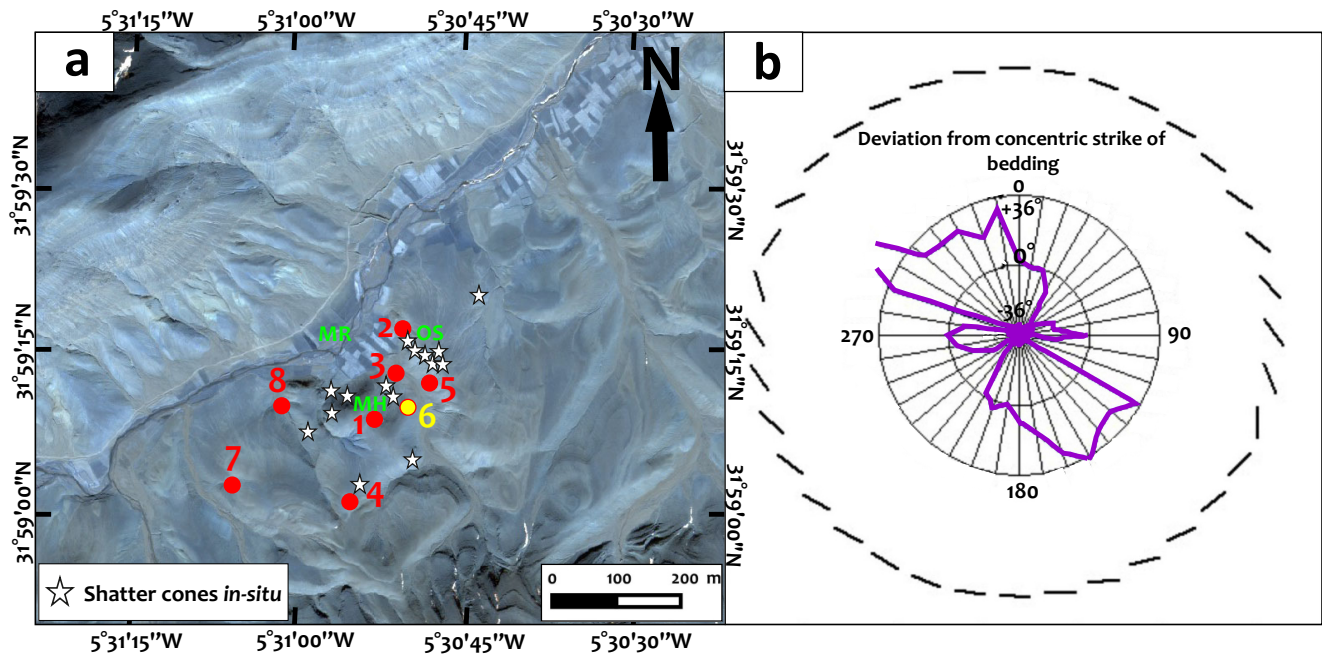


Fig. 9. a) Location of the eight points used for the application of the concentric deviation method. These points are a selection of possible centers of the Agoudal impact structure, plotted on a satellite image WorldView-2 of the studied site of Agoudal. “OS,” “MR,” and “MH” abbreviations refer to the vertical to overturned strata, the “Main River,” and the “Main Hill,” respectively. b) Polar plot corresponding to the deviation of bedding orientation from concentric strike associated with the lowest deviation from concentric strike bedding (point 6; $31^{\circ}59'13.73''$ N and $5^{\circ}30'55.14''$ W). Azimuth values range from 0 to 360°. The azimuth gives the angular location relative to the crater center (e.g., a data point directly north of the center has a value of 0°, east has a value of 90°, etc.). The purple curve is the concentric deviation curve. It indicates the deviation of bedding strike from the tangent to a hypothetical circle centered on the center of the crater. Bars of average strike around polar plots are based on the values of the concentric deviation curve and are used to enhance the interpretation of the data. Positive concentric deviation values represent clockwise rotation from concentric strike; negative values correspond to counterclockwise rotation. To improve the interpretation of the data, 36 black bars of average strike were added around the polar plot in steps of 10°, oriented according to the concentric deviation after smoothing with the “overlapping bins” method. The rotation is shown with a twofold factor of exaggeration. The polar plots corresponding to the deviation from concentric strike bedding for the seven other input points are given in Material S1. (Color figure can be viewed at wileyonlinelibrary.com.)

Orientation data of bedding planes are shown in Figs. 8a–c, while the orientation data of faults and joints related to the regional High Atlas fracture systems, including the Tertiary Alpine shortening (Frizon de Lamotte et al. 2008; Michard et al. 2011), and the deformation systems related to the impact cratering event shown in Figs. 8d–f. The orientations of fault and fracture planes within the Agoudal area are similar to the fracturing observed in the High Atlas and particularly in the Imilchil transect, with two major sets of fracturing: a N–S set and a ~N80–90 set (Ibouh 1995; El Moudjahid et al. 2016). At the “Main Hill,” the stereographic projection in Fig. 8a shows mainly strata dipping steeply toward the east to south.

The concentric deviation method was applied for eight test points. The points were selected within the disturbed zone and within the observed maximum spatial extent of in situ SCs. For each point, we have considered the entire set of collected strike

measurements of the bedding planes of the central zone, where SCs in situ and vertical to overturned strata are reported. The lowest degree of deviation from pure concentric strike is found if the center is placed in the “Main Hill” (noted “MH” in Figs. 9a and 9b) at $31^{\circ}59'13.73''$ N, $5^{\circ}30'55.14''$ W (point 6) (Figs. 9a and 9b). The other selected points (presented in Material S1 in supporting information) show a significantly higher degree of deviation from pure concentric strike compared to point 6.

Geological Map and Cross Sections

Our lithological and structural observations are reported here on the first geological and morphological map of the Agoudal impact structure, at a scale of 1:30,000 (Fig. 10a). A more detailed map is given over the central area at a scale of 1:15,000 (Fig. 10b). Six cross sections of the Agoudal impact site are presented

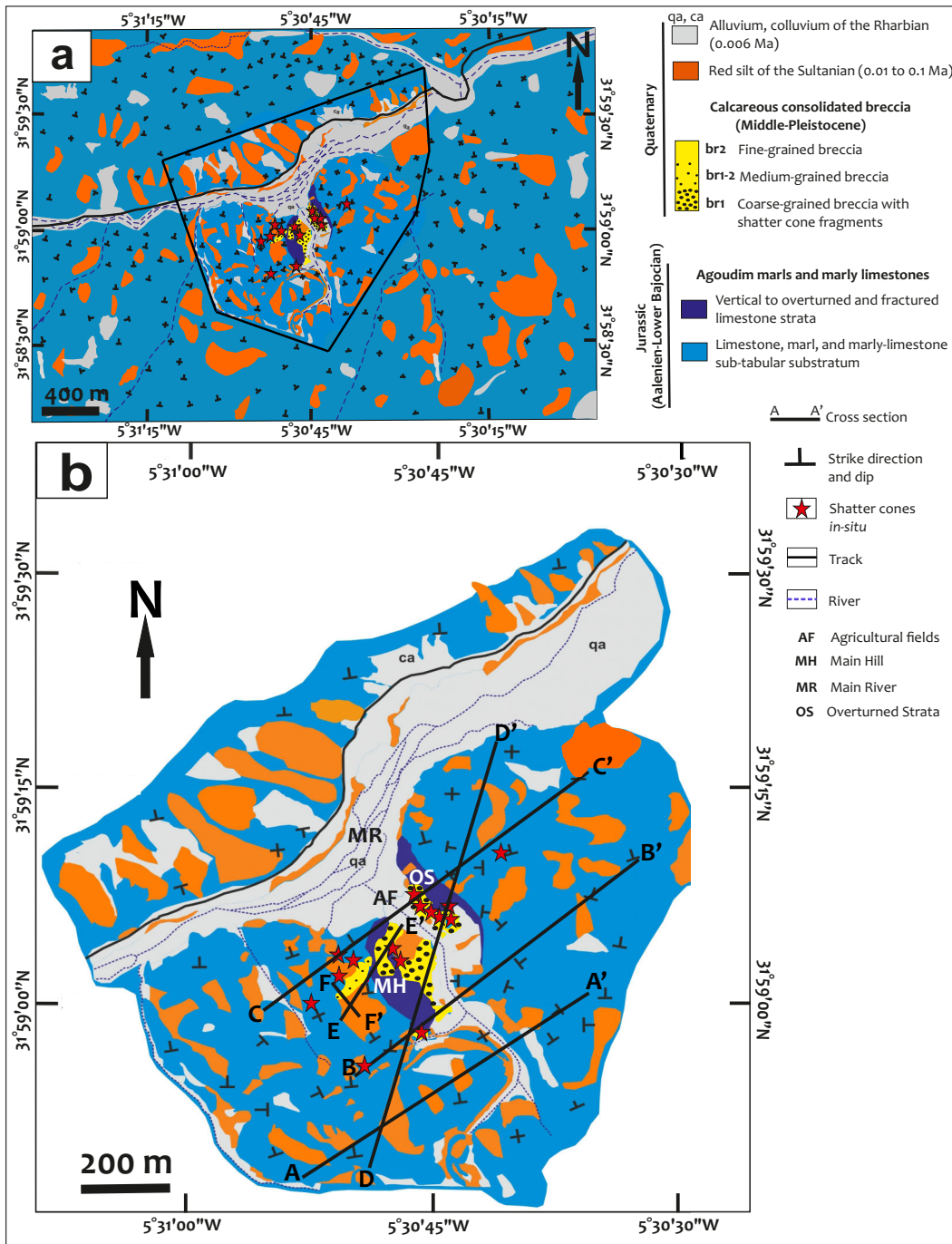


Fig. 10. a) Geological map of the Agoudal impact site, covering an area of 6 km², with the polygon of the central area represented in (b). b) Geological map of the central area. The disturbed region has an area of about 2.25 km². It includes shatter cones, vertical to overturned strata (in dark blue color), and breccias, with the localization of six schematic cross sections. c) Six cross sections in WSW–ENE direction (A–A'; B–B'; C–C'), SSW–NEE direction (D–D' and E–E'), and NNW–SSE direction (F–F'). Note that Agoudim marls and marly limestones are not represented at the river location, as there is no clue of their trending under the river bed. (Color figure can be viewed at wileyonlinelibrary.com.)

in Fig. 10c. Their locations are shown on the close-up view on Fig. 10b. They are oriented in different directions: WSW–ENE (A–A', B–B', and C–C'), SSW–NNE (D–D' and E–E'), and NNW–SSE (F–F'). A–A'

intersects the southern part of the area which is tectonically deformed by the Atlas orogenic shortening but does not show any disturbance related to the impact, and also does not show SCs in floats or in

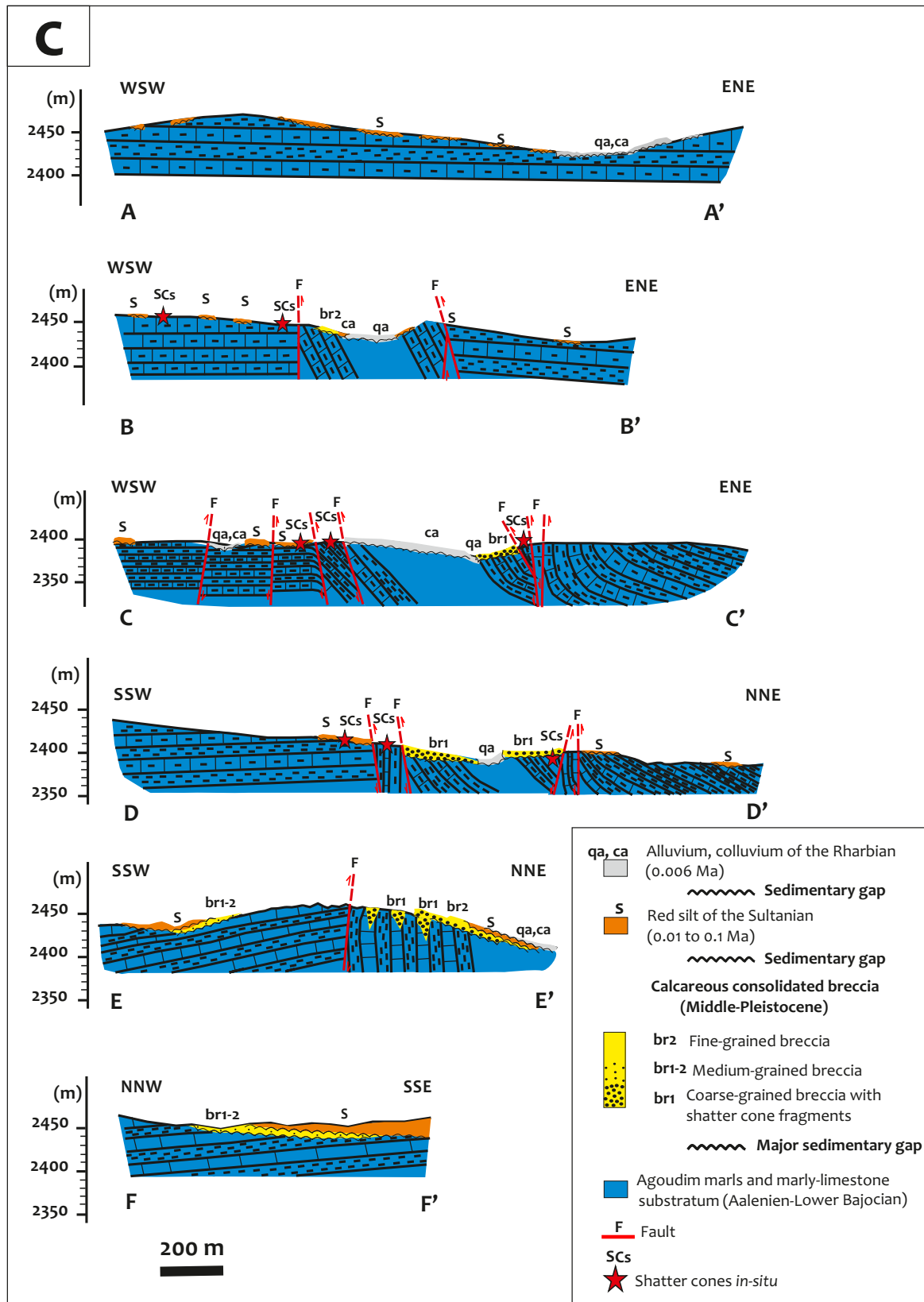


Fig. 10. c) Six cross sections in WSW-ENE direction (A–A0; B–B0; C–C0), SSW–NNE direction (D–D0 and E–E0), and NNW–SSE direction (F–F0). Note that Agoudim marls and marly limestones are not represented at the river location, as there is no clue of their trending under the river bed. (Color figure can be viewed at wileyonlinelibrary.com.)

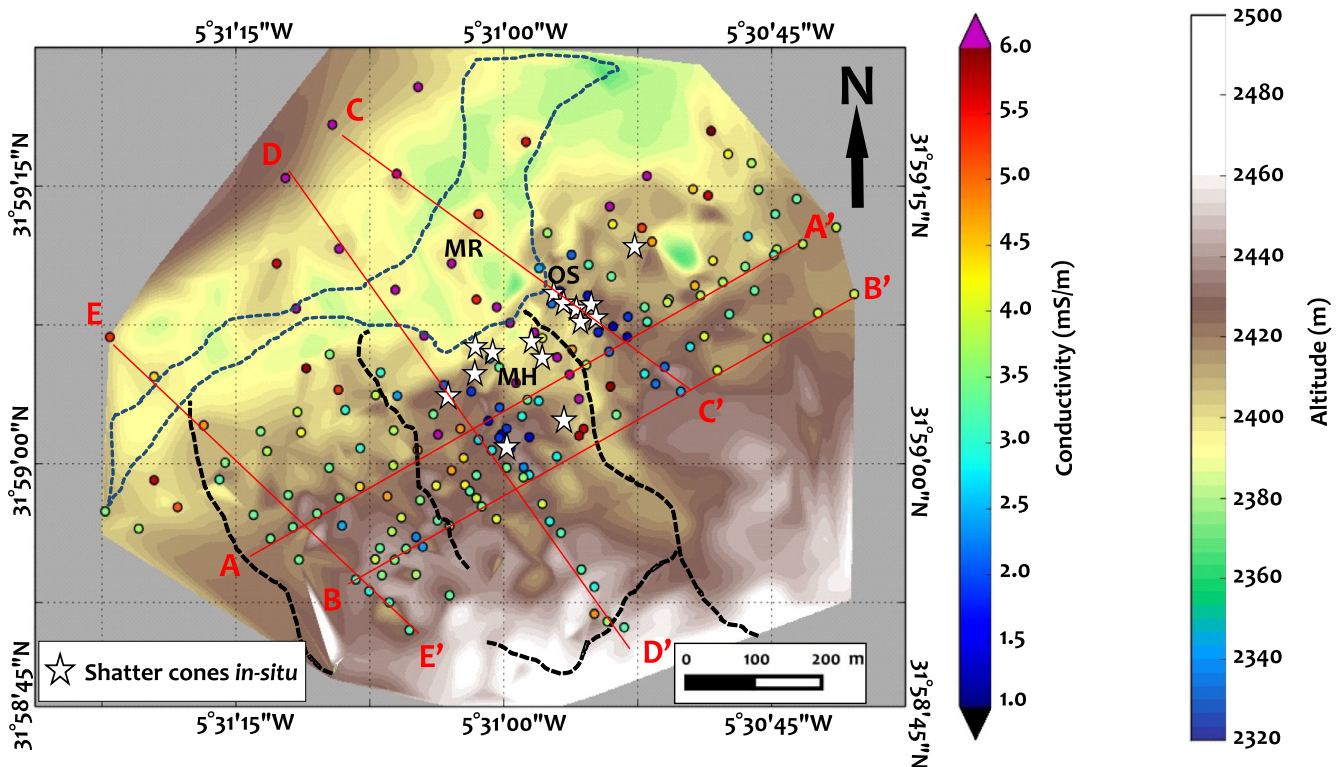


Fig. 11. Conductivity map of the Agoudal impact structure superimposed on the topographic image. See color scale for conductivity values. Values less than 1 mS/m are shown in black and values in excess of 6 mS/m are shown in purple. Five cross sections of the apparent conductivity in ENE–WSW direction (A–A' and B–B') and in the NW–SE (C–C'; D–D' and E–E') are presented in Fig. 12. “OS,” “MR,” and “MH” abbreviations refer to the vertical to overturned strata, the “Main River,” and the “Main Hill,” respectively. (Color figure can be viewed at wileyonlinelibrary.com.)

outcrops. The cross sections B–B' and C–C' are drawn across the central area (“Main Hill”), which is associated with local structural disturbances, the three types of breccias, the main outcrops of SCs, and the vertical strata discovered recently at the “Main Hill.” D–D' highlights the disturbance of the central area. It includes the SC outcrops, the breccias, and the vertical to overturned strata, as well as the fault system related to the impact event. E–E' shows the three types of breccias, especially “br1” (unclear origin), and the succession of the Quaternary terrains (red silts, alluviums, and colluviums). The transition from the subtabular area to the disturbed area is also reflected in the cross section E–E'. The cross section F–F' shows a tabular domain within the disturbed area and the transition from Jurassic formations to the fine-grained breccias and eventually the Quaternary red silts of the Sultanian formation.

Conductivity Mapping and Profiles

In Fig. 11, an apparent conductivity map at 15 m depth is superimposed on the topographic image of the

studied area. Although the “Main River” is generally dry (“wadi”), some water wells for irrigation, located nearby, indicate permanent groundwater reservoirs under the riverbed.

The five cross sections of apparent conductivity (Fig. 12), and the 3-D representation (Fig. 13), show that the river floor and valleys are relatively conductive ($>5 \text{ mS m}^{-1}$, red and purple colors) whereas the terrace is relatively resistive ($<5 \text{ mS m}^{-1}$, yellow to blue colors). Since the conductivity is sensitive to the water content, this distribution can be explained by the existence of groundwater under the riverbed and valley. In the 3-D representation, resistive blocks (blue colored, $<2 \text{ mS m}^{-1}$) may be noted at a depth shallower than 15 m (elevation ranging from 2380–2410 m) in the center of the terrace (see blue areas in A–A', C–C', and D–D'). The resistive areas are not necessarily correlated with elevation, but correlate well with the areas of occurrences of breccias and SCs. These resistive blocks may be part of a circular anomaly of 350 m in diameter of resistive material. However, it is not possible to conclude on the circular nature of the anomaly given the erosion at the NW and SE sectors.

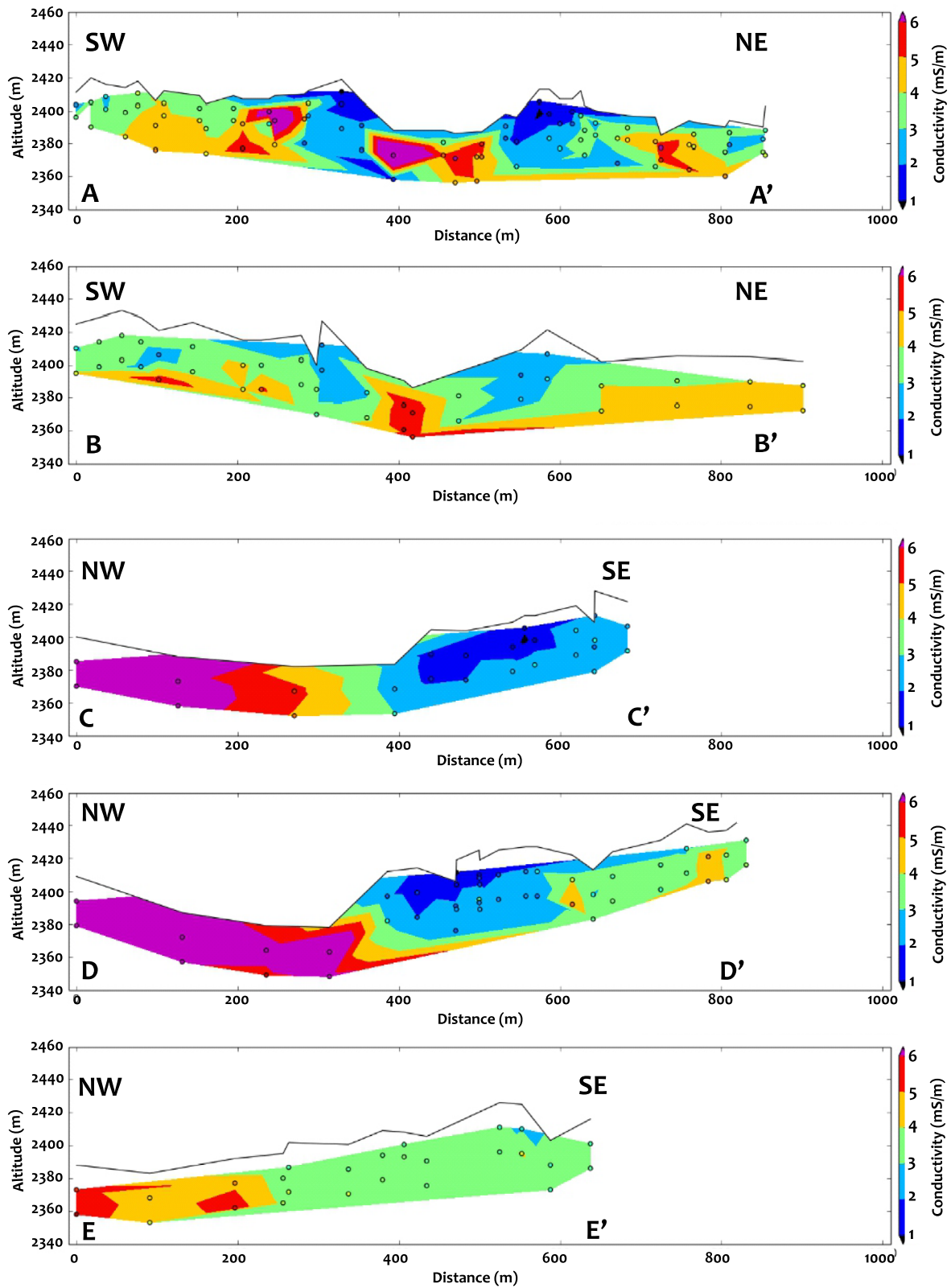


Fig. 12. Five cross sections of the apparent conductivity in WSW–ENE direction (A–A' and B–B') and NW–SE direction (C–C'; D–D'; and E–E'; see Fig. 11 for the location of the sections). The values are represented with six color levels and values outside the color scale are represented in black ($<1 \text{ mS m}^{-1}$) and purple ($>6 \text{ mS m}^{-1}$). (Color figure can be viewed at wileyonlinelibrary.com.)

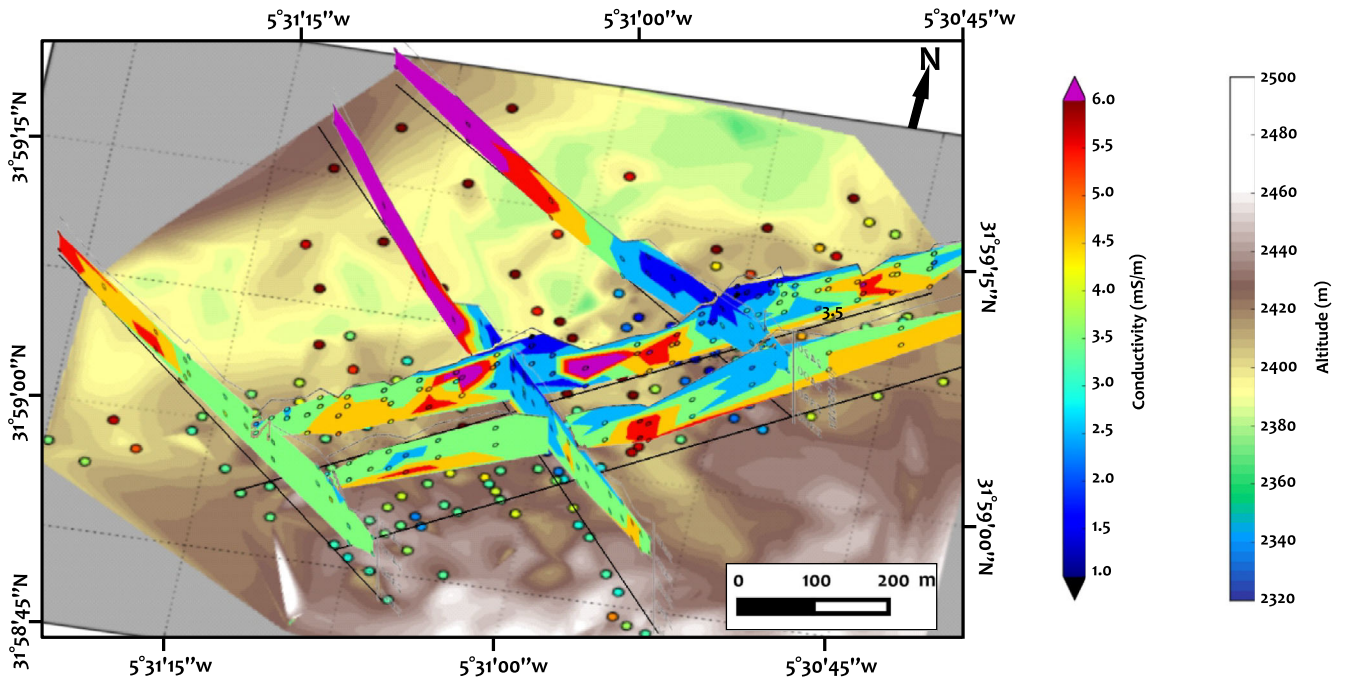


Fig. 13. 3-D representation of the cross sections of conductivity at the Agoudal area. (Color figure can be viewed at wileyonline library.com.)

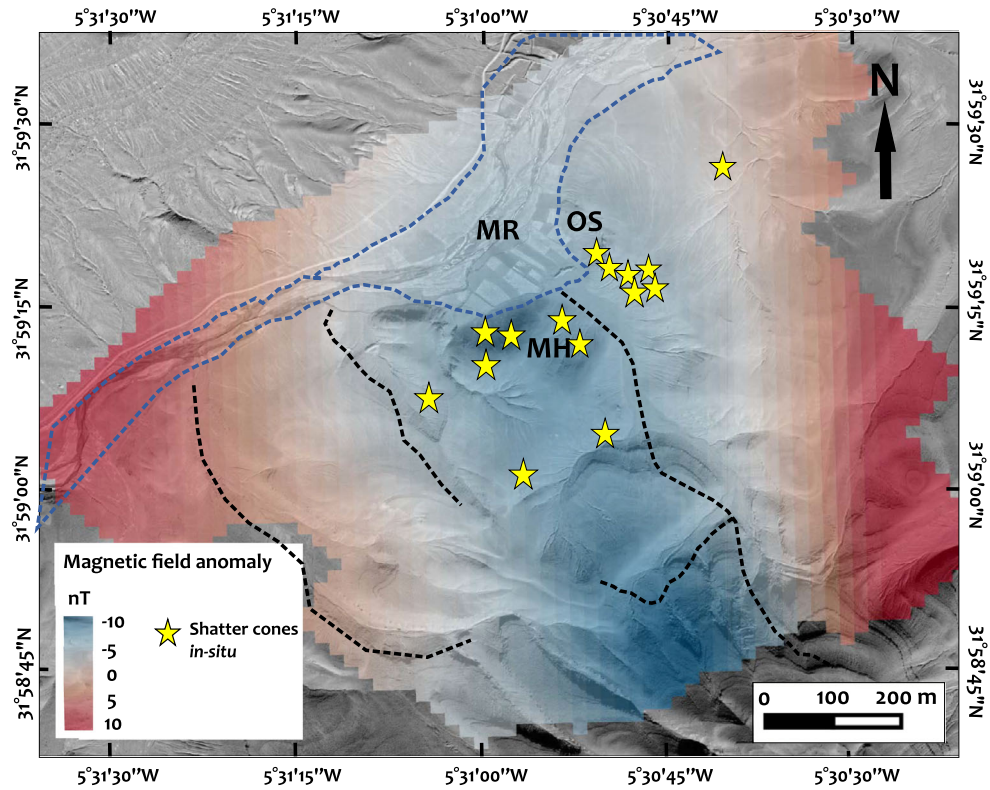


Fig. 14. Map of the reduction-to-the-pole (RTP) magnetic field anomaly of the Agoudal area. “OS,” “MR,” and “MH” abbreviations refer to the vertical to overturned strata, the “Main River,” and the “Main Hill,” respectively. (Color figure can be viewed at wileyonlinelibrary.com.)

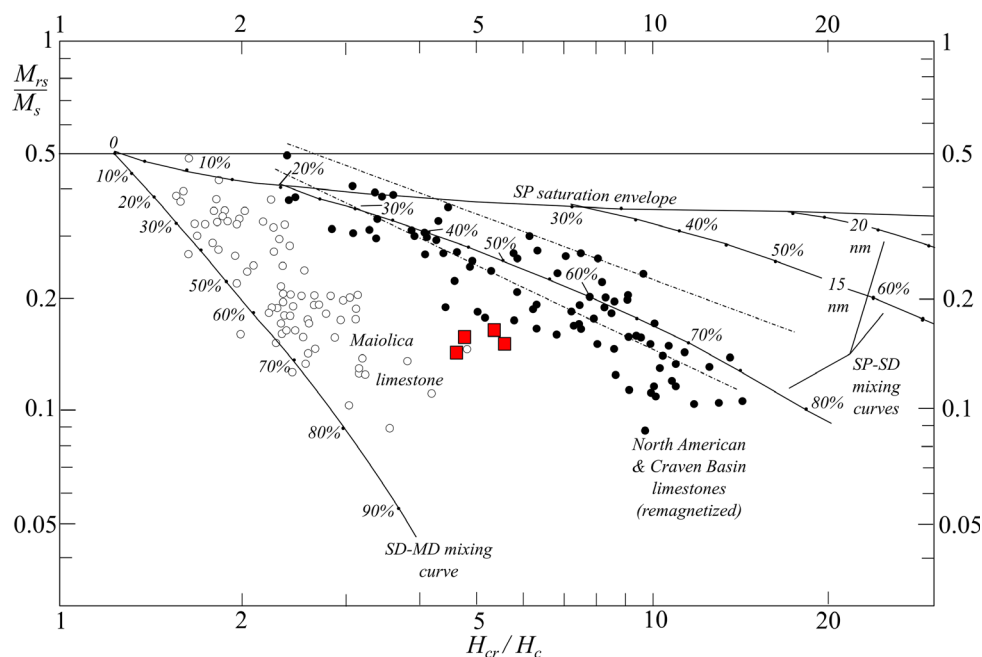


Fig. 15. Agoudal magnetic mineralogy evaluated using hysteresis parameters measured from Agoudal samples AGC, AGD, AGG, and AGL (red squares) and the theoretical curves of Dunlop (2002). Abbreviations: M_{rs} = saturation remanence; M_s = saturation magnetization; H_c = coercivity; H_{cr} = coercivity of remanence; SD = single-domain; MD = multidomain; and SP = pseudo-single domain. (Color figure can be viewed at wileyonlinelibrary.com.)

Magnetic Field Mapping

The RTP magnetic field anomaly map (Fig. 14) shows a general negative signal (-10 nT) in the central and southern part of the studied area, while a positive anomaly is found in the eastern and western parts of the magnetic map. The negative anomaly area occurs at the top of the central hill (MH) where the main SC outcrops and breccias are located, but also south from this “MH.” The positive anomaly signal ($+10$ nT) coincides with areas where the layers are subtabular. These subtabular layers are dominated by colluviums of the Rharbian period as well as red silts of the Sultanian. The applied analytical signal (AS) technique (Blakely 1995) unveils the location of the magnetized sources which cause the RTP low magnetic anomaly (Material S2 in supporting information). A positive AS area clearly corresponds to the “Main Hill.” Therefore, our magnetic data support a possible association between the “geologically disturbed” area in Agoudal (mainly SC area and “MH”) and the magnetic low which extends toward the south.

Rock Magnetism

Magnetic susceptibility measurements were carried out to support the interpretation of the magnetic anomalies. The dark limestone shows a rather

homogeneous value at $1.5 \pm 0.6 \times 10^{-3}$ SI. Hysteresis measurements on +4 samples (AGC, AGD, AGG, and AGL) show that paramagnetic clays account for only $25 \pm 3 \times 10^{-6}$ SI. Based on hysteresis parameters ($M_{rs}/M_s = 0.16$, $H_{cr}/H_c = 5$ with $H_{cr} = 38$ mT, see Fig. 15), ferromagnetic contribution appears to be carried by magnetite, with domain state from superparamagnetic to pseudo-single domain. Assuming pure magnetite, the measured M_s (13.5 ± 3.3 mA m² kg⁻¹) corresponds to 150 ppm of magnetite.

However, in two SC-bearing sites (AGC and AGG) (Fig. 4), the limestone appears white to yellowish, suggesting secondary oxidation of pyrite. In the limestone as well as in the breccia samples, this oxidation leads to a much lower susceptibility of $220 \pm 80 \times 10^{-6}$ SI on average, which is interpreted as the breakdown of magnetite.

Natural remnant magnetization intensity varies in gray limestone outcrops between 10 and 83 mA m⁻¹. Its direction before demagnetization appears close to PDF, allowing to estimate total in situ magnetization by simple scalar addition of NRM and K multiplied by the PDF intensity. The Koenigsberger ratio of remnant over induced magnetization is on average 0.7 ± 0.4 . Total average magnetization is 84 ± 40 mA m⁻¹. In the two oxidized limestone outcrops as well as in the breccia, NRM intensity is lower (5.5 ± 0.8 mA m⁻¹) leading to a total magnetization of 11 ± 5 mA m⁻¹.

Therefore, the process of surface fragmentation and oxidation, enhanced at depth in the SC bearing fractured zone, may lead to a negative magnetic anomaly associated with a magnetization decrease of $73 \pm 45 \text{ mA m}^{-1}$. Such a layer is indeed able to generate a magnetic anomaly low of the order of -10 nT (Fig. 14). The magnetic anomaly is too poorly defined to estimate a layer thickness.

Cosmogenic Nuclides

The sample concentrations inside the area with SCs and at a distance of 5 km from this area were found to be of 4.67 and $9.76 \cdot 10^5 \text{ atoms } ^{36}\text{Cl g}^{-1}$, respectively. This translates into denudation rates of 430 and 220 m Ma^{-1} (with a 10% uncertainty), respectively (see Schimmelpfennig et al. 2009). These reported erosion rates are 10 times higher than average rates observed for the carbonate plateau around the Mediterranean Sea (from 17 to 19 m Ma^{-1} in the Mediterranean semiarid zones to 21 – 25 m Ma^{-1} in the hyperarid zone; Ryb et al. 2014). Moreover, this erosion rate is higher than the erosion rate of 80 m Ma^{-1} inferred from apatite fission-track thermochronology for the Neogene, or similar denudation rates of 80 m Ma^{-1} (0.08 mm yr^{-1}) estimated for the Anti-Atlas region (Ruiz et al. 2011).

DISCUSSION

Discussion of the Geological and Structural Data

Although no circular structure is observed on remote sensing data or inferred from structural or geological observations around the SC locations, the combined geological, structural, and geophysical data reveal a disturbed area. Considering that the surrounding bedding layers are subhorizontal and are characterized by the most common strike trends in the Atlas ($\text{N}70^\circ$; Ibouh 2004), the vertical and overturned strata represent an anomaly with respect to the tectonic history. They are therefore interpreted as target rocks that were tilted during the excavation or collapse phase of the impact cratering event. Furthermore, both sides of the anticlinal ridges (Figs. 2a and 2b) surrounding Agoudal show an average dip of 25 – 45° toward the north or south (Ibouh and Chafiki 2017). The occurrence of vertical bedding at a synclinal zone between two ridges, which is found at the Agoudal site, is anomalous. The fine fracturing noticed in the vertical layers appears to be exclusively related to the disturbed area and not related to the major Atlas-age folds. It is of note that the best candidate for the location of the center of the crater, based on the deviation from

concentric strike, is located in the “Main Hill.” This is concordant with the structurally most disturbed area and the occurrence of SC outcrops.

The breccia “br1,” which is distinct from the consolidated scree slopes “br2” and “br1-2,” is only present in the disturbed zone. It also includes fragments of SCs. The earlier hypothesis that this breccia is an impact product (Lorenz et al. 2015) is not confirmed by the present study, but is not ruled out either. The “br1” breccia could be a lithic monomict impact-related breccia, taking into consideration that lithic monomict breccias do not systematically show shock metamorphic overprint or impact melt rock (Stöffler and Grieve 2007). Moreover, monomict brecciation occurs frequently at impact craters (Stöffler and Grieve 2007). Considering that SC fragments contained in “br1” are scattered and oriented in different directions, the event responsible for SC formation is older than the emplacement of the breccia deposit.

Discussion of Geophysical Signatures

The interpretation of the geophysical signatures of largely eroded impact structures and inferences on the size of the structure may be challenging. In the extreme case of the small and old (455 Ma) meteorite impact crater of Kärddla (4 km diameter, Estonia), the geophysical properties of rock samples that are situated at large depths with respect to the eroded crater floor are similar to those of unshocked target rocks (Plado et al. 1996). Indeed, the effects of shock on geophysical properties are best seen in the rocks of the crater floor (impact breccias), not in those at larger depths. The central uplift of the Kärddla impact structure, as shown by drill core data, has no observable geophysical signal (Plado et al. 1996).

At Agoudal, the magnetic low coincides well with the disturbed main hill (MH), where the main SC outcrops and breccias are located, as well as south of the MH. This might be due to the impact event that has reduced the target rock magnetization. The positive anomaly signal ($+10 \text{ nT}$) coincides with areas where the layers are subtabular. A larger survey may be necessary to confirm the origins of the magnetic patterns. However, in the case of the electric conductivity, a resistive anomaly is correlated with the SC occurrence area and the vertical to overturned layers trending $\text{N}150$ – $\text{N}160$, which are not related to the major Atlas deformation. High conductivity is observed at the “Main Hill” (MH, Fig. 11) where many SC outcrops and thick breccia deposits are located as well as in the valleys and in the NNW area. The resistive areas and the conductive material in the subsurface of the “Main River” are therefore hypothesized to be part of the impact structure.

In general, the main change in the electrical properties of the target rocks due to the impact is an increase in conductivity due to the fracturing of the rock increasing porosity and, more importantly permeability, allowing a current to be carried by ions in pore fluids (Hawke 2004). Low resistivity, associated with fracturing of crystalline target rocks and postimpact crater fill, was identified at the Saarijärvi impact structure (Pesonen et al. 1998). The electrical mapping at Saarijärvi has shown half of a possible circular feature, while the area where the other half could be observed is covered by a lake (Pesonen et al. 1998). A positive anomaly of electric conductivity was also identified at the Karikkoselkä impact structure (Pesonen et al. 1998). In both examples, the conductivity is due to the fracturing within the substructure of the crater which might also be the case at the Agoudal impact site.

Discussion of Denudation Rates

The rapid erosion determined by ^{36}Cl measurements, which is in the $220\text{--}430\text{ m Ma}^{-1}$ range, is consistent with the high altitude and rough topography favoring erosion by meteoric water, snow melting floods, and cryoclastic processes associated with successions of freeze–thaw cycles. Considering that SCs occur within an area of $1/2\text{--}1/6$ of the impact crater's original diameter (Baratoux and Reimold 2016), the SC outcrop area of $700 \times 400\text{ m}$ in the Agoudal impact structure supports an original crater diameter of $1.4\text{--}4.2\text{ km}$. This diameter should be associated with an original topographical relief of $\sim 140\text{ to }420\text{ m}$ ($1/10$ of the crater diameter; Melosh 1989). Using the new estimates of Agoudal erosion rates of $220\text{--}430\text{ m Ma}^{-1}$, the morphologic expression would be completely eroded within $0.3\text{--}1.9\text{ Ma}$. Moreover, we observed the presence of long dead cedar stump on the top of the main SC hill, indicating that a forest was once present above the crater. Anthropogenic destruction of this forest in the last millennia may account for accelerated erosion and soil disappearance. In fact, remnants of yellowish thick soil or scree mantle are visible on both sides of the valley. Such formations are lacking in the crater area.

Higher erosion or incision rates needed to erase a 1-km crater in about $100,000\text{ yr}$ (the age of Agoudal iron meteorite) would not be consistent with the widespread preservation of reasonably freshly preserved iron fragments of the meteorite of Agoudal. These considerations further refute a coeval impact event associated with the SCs and the Agoudal meteorite fall. A fall onto a previously formed impact crater appears surprising. However, such coincidental events have been reported elsewhere (Aouelloul structure, according to

Fudali and Cressy 1976; Rio Cuarto, according to Levine et al. 2007) and are not impossible from a statistical point of view (see the discussion by Chennaoui Aoudjehane et al. 2016).

Stratigraphy and Chronology of Events at the Agoudal Impact Site

The stratigraphy of the Mesozoic–Cenozoic series of the Central High Atlas is summarized in Figs. 2 and 3, and is reflected in the cross sections of Fig. 10c. The chronology of events that took place in the Agoudal site is presented in Fig. 16. They may be described as follows:

1. Deposition of Mesozoic sedimentary sequence.
2. A major discontinuity corresponding to a huge time gap (55 Ma , Paleocene–Eocene boundary, to 0.8 Ma , Middle Pleistocene) and an important erosion.
3. The major Atlas orogeny in the Upper Eocene and Neogene (between 37 and 10 Ma).
4. The impact event: formation of an impact crater with a diameter of $1.4\text{--}4.2\text{ km}$, formation of SCs, and vertical to overturned strata ($1.9\text{--}0.3\text{ Ma}$).
5. Postimpact erosion, removing hundreds of meters of Bajocian sediments and exposing the Agoudal SCs.
6. Formation and consolidation of breccias. The formation and consolidation of coarse-grained calcareous breccia deposits “br1” ($\geq 10\text{ cm}$) occurred in the central disturbed area, filling fractures and including scattered SCs fragments. If this breccia was impact related, it formed within a few seconds after the impact event in the crater basement. The formation and consolidation of fine-grained breccia “br2” deposits (fragment size $< 1\text{ cm}$) occurred in the southern part of the disturbed area (Fig. 10b). The medium-grained breccia “br1-2” is localized in the western area (profiles E–E' and F–F'; Fig. 10c). The “br2” and “br1-2” types of breccia, beneath the Sultanian red silts, are attributed to the Amirian–Tensiftian ages of the Moroccan Quaternary epoch (Middle Pleistocene, between 0.781 and 0.126 Ma). The “br2” breccia is found deposited on top of the “br1” breccia. Hence, “br1” is older than “br2,” and “br1-2” is an intermediate breccia to “br1” and “br2.” The three types of breccias seem to be related. They are considered as Quaternary sedimentary cemented colluvium. The different brecciation events and consolidation of breccias deposits might have occurred in a short period of time.
7. Erosion period corresponding to an important sedimentary gap with a radical climate change between hyperhumid periods with generalized runoff

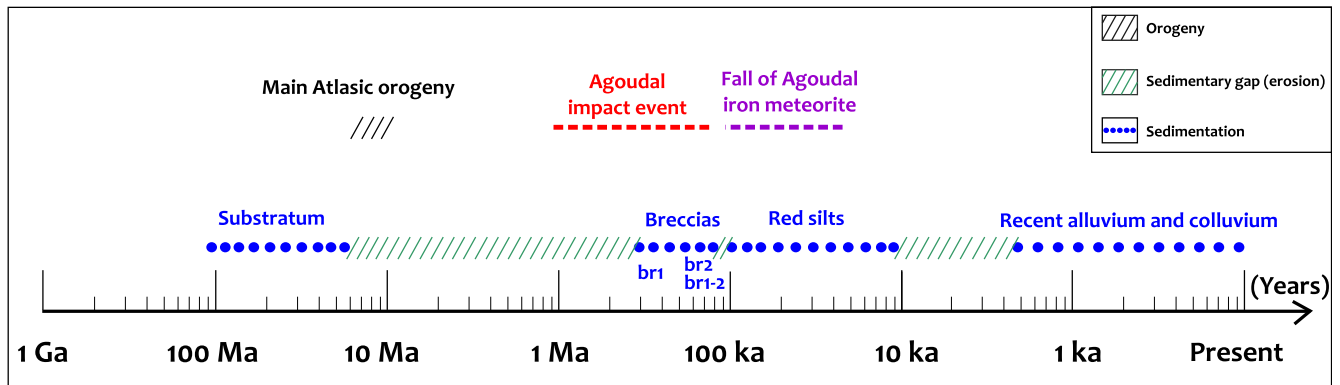


Fig. 16. Chronology of events at the Agoudal impact site. (Color figure can be viewed at wileyonlinelibrary.com.)

- on the slopes, and a subsequent period with a tropical climate allowing the formation of red oxides (Early Pleistocene, between 2.5 and 0.7 Ma).
8. Formation of red silt deposits, reaching several meters thickness, during the Sultanian (Upper Pleistocene, between 0.1 and 0.01 Ma).
 9. Fall of the Agoudal iron meteorite (0.105 ± 0.040 Ma; Hutzler et al. 2014; Hutzler 2015).
 10. Erosion period corresponding to an important sedimentary gap marking the end of the oxidizing tropical period and the beginning of the current temperate period (Rharbian, 0.006 Ma; Beaudet et al. 1967).
 11. Nonconsolidated colluvial deposits connected with the alluvium of the bottom of the thalwegs (0.006 Ma to present).

Comparison of Agoudal Impact Structure with Santa Fe Impact Structure and Steinheim Crater

The Santa Fe impact structure, ~8 km northeast of the city of Santa Fe, New Mexico, USA, was confirmed by the occurrence of meter-sized SCs in Paleoproterozoic crystalline rocks exposed over an area of 5 km² (Fackelman et al. 2008). There are notable similarities between Santa Fe and the site of Agoudal. As with Agoudal, the Santa Fe impact structure does not show any circular expression in the topography of satellite imagery (Montalvo et al. 2018).

Santa Fe was identified following the fortuitous observation of SCs by Thornton H. McElvain during field work in 2005 (Fackelman et al. 2008). These meter-sized SCs are well developed, facilitating their discovery, contrary to the centimeter-sized well-developed SCs of Agoudal. As for Agoudal, SC occurrences are assumed to represent the remnants of

the central uplift of an eroded crater. Several SCs were also found in float rocks, suggesting a large area of occurrences. The diameter of 6–13 km (Fackelman et al. 2008) is based on the extent of SC occurrences. At least three different types of breccias have been reported at Santa Fe (Wright et al. 2010; Wright and Cavosie 2017) and their origin is unclear, as in the case of Agoudal. The breccias are interpreted as the remnants of impact and/or fault breccias by Wright and Cavosie (2017). In contrast to the impact-related vertical to overturned strata in Agoudal, no evidence for impact-related tectonic deformation has been reported at the macroscopic scale. Moreover, reported tectonic deformation after the impact event at Santa Fe and the complex tectonic context do not facilitate the identification of impact-related deformation (Montalvo et al. 2018). The age of the Santa Fe impact structure is not known, although the lack of circular features, the absence of geophysical signatures, and the evidence of postimpact tectonic deformation do suggest that the impact is ancient. This situation is considered to be similar to the case of the Agoudal impact structure, where the structural features, including vertical to overturned strata, the area of SCs, and the breccia occurrences may be the relict of a central uplift of a deeply eroded complex impact structure.

The distribution of SCs at Agoudal and their relation to the impact structure may also be analyzed based on the comparison with the Steinheim impact structure, which has comparable dimension (3.8 km in diameter), but is less eroded despite an age of 15.1 ± 0.1 Ma. SCs are developed in Jurassic limestones at both impact structures, and are exclusively associated with the central uplift in the case of Steinheim. The size of SCs from both structures is similar. This observation supports the hypothesis that the SCs at Agoudal are

associated with the central uplift of the structure, even if its topographic expression has been erased.

CONCLUSIONS

The discovery of the first impact structure in Morocco was made by the fortuitous observation of well-preserved SCs during a meteorite search campaign. Their distribution within the disturbed area, as well as the location of vertical and the overturned strata along with breccias, is documented in the first geological map of the Agoudal impact structure at the scale of 1:30,000. The general map covers an area of 6 km² and shows the relationships between the nondisturbed subtabular Jurassic marl and limestone formations with a central disturbed area. The central area of 2.25 km² is documented in a detailed map at a scale of 1:15,000. The map of dip angles of the central area with SC outcrops shows a disturbed zone of 0.15 km² with two domains of enhanced dipping corresponding to the vertical and overturned strata observed in the field. A dip azimuth map shows that these perturbations correlate with the SC area. The fracturing and stratification within this area are also disturbed. The center of original impact crater was determined using the concentric deviation technique and is located in the “Main Hill” (31°59′13.73″N, 5°30′55.14″W). Furthermore, the location of electromagnetic anomalies and negative magnetic anomalies also correlate with the location of SCs and breccias. One of the three breccias types (br1) might be impact related, though no direct evidence was found (impact melt rock) to make a definitive conclusion. The Agoudal breccia requires further detailed petrological studies and geochemical analysis, especially considering that breccia samples from the main outcrop were reported to contain partly oxidized fragments from the iron meteorite and relics of weathered impact melt rocks by Lorenz et al. (2015). Schmieder et al. (2015) has also reported traces of the Agoudal iron meteorite on the surface of SCs from the Agoudal impact site.

We conclude that Agoudal SC occurrences are associated with a single impact structure. The topographic expression of this structure is now eroded. The traces of this impact event include SCs and geophysical anomalies related to the impact event. Despite high-resolution geological and geophysical mapping, it remains difficult to constrain the exact size and the complex or simple nature of the impact structure. In the case of a simple crater, the vertical to overturned strata could correspond to a remnant of a crater rim, but SCs are not expected in the crater rim of a simple crater. For a complex crater, the structural features and area of SC and breccia occurrences may be

the relict of a central uplift, and the “Main Hill” location would represent the center of the remnant of a deeply eroded impact structure. As SCs are not unambiguously reported for structures smaller than 1 km in diameter (Baratoux and Reimold 2016) and from the fact that they generally occur within an area corresponding to 1/6–1/2 of the estimated original diameter of the impact crater, and considering the newly calculated erosion rates in Agoudal (220–430 m Ma⁻¹), the original impact crater of Agoudal has more likely a diameter of 1.4–4.2 km and an age of 0.3–1.9 Ma. These new results are in concordance with the estimated size of 1–3 km and a minimum age of 1 Ma based on the Anti-Atlas erosion rates (80 m Ma⁻¹; Ruiz et al. 2011), proposed by Chennaoui Aoudjehane et al. (2016).

Since the presence of SCs in the rim area of a simple crater is unlikely, we favor the interpretation that the area of SC occurrence may be the relict of a central uplift where the rest of the crater has been eroded. This assertion is also supported by the comparison with the Steinheim impact structure, and is similar to the interpretation made of the SC occurrences at the Santa Fe impact structure. The current estimates of erosion rates of 430–220 m Ma⁻¹ inside the impact site and 5 km SE of the disturbed area, respectively, allow removing hundreds of meters per million years. These erosion rates are sufficient to completely wipe out any crater extending from 1.4 to 4.2 km in diameter within a calculated period time of 0.3–1.9 Ma. Given the relative chronology of deposits, we confirm that the impact event and the Agoudal meteorite fall are two chronologically distinct events (Chennaoui Aoudjehane et al. 2016). A better understanding of the SC formation mechanism and factors controlling their morphological parameters is critical to elucidate the size of largely eroded impact structures (Baratoux and Reimold 2016). Deeply eroded impact structures may become the most common situation in future discoveries.

Acknowledgments—This research is part of a continental-wide initiative, the African Initiative for Planetary and Space Science (<http://africapss.org>). Part of this initiative supports the development and promotion of planetary science and meteoritics. Brahim Hdach, Ait Rhou Moha, Ait Rhou Bassou, and Nacer Hdach are warmly thanked for their constant and precious help during the different field trips to Agoudal since 2013. We also express our special thanks to Prof. Tihomir Marjanac, from the University of Zagreb-Croatia, for his help providing access to the CorelDraw-6 software and to the facilities at the Faculty of Sciences of Zagreb, and for fruitful discussions. We

acknowledge the European Erasmus Mundus (EU Metallic II 7892) scholarship program (Hassan II University of Casablanca Morocco and Zagreb University, Croatia) and Erasmus + (Hassan II University of Casablanca and Université Pierre et Marie Curie Paris 6) for financial support. This research has also been partly funded by the Partenariat Hubert Curien/Volubilis Program (PHC24675QJ, Impact rate in the Earth-Moon System) and by CNRS/INSU (Programme National de Planétologie). The IRD representation in Morocco is also thanked for providing a 4 × 4 vehicle for field work in 2018. Associate editor C. Koeberl and reviewers A.P. Crósta, an anonymous reviewer, and W.U. Reimold are thanked for their detailed reviews and for constructive comments.

Editorial Handling—Dr. Christian Koeberl

REFERENCES

- Amrhar M. 1995. Tectonique et inversion géodynamiques post-rift dans le Haut Atlas occidental: Structures, instabilités tectoniques et magmatisme liés à l'ouverture de l'Atlantique central et la collision Afrique-Europe. Ph.D. thesis. Cadi Ayyad University of Marrakech-Morocco. 253 p.
- Baratoux D. and Reimold W. U. 2016. The current state of knowledge about shatter cones genesis: Introduction to the special issue on shatter cones. *Meteoritics & Planetary Science* 51:1389–1434. <https://doi.org/10.1111/maps.12678>.
- Baratoux D., Niang C. A. B., Reimold W. U., Selorm Saph M., Jessell M., Boamah D., Faye G., Bouley S., and Vanderheaghe O. 2019. Bosumtwi impact structure, Ghana: Evidence for fluidized emplacement of the ejecta. *Meteoritics & Planetary Science* 54:1–16. <https://doi.org/10.1111/maps.13253>.
- Beudet G., Maurer G., and Ruellan A. 1967. Le Quaternaire Marocain: observations et hypothèses nouvelles. *Revue de Géographie Physique et de Géologie Dynamique* 4:269–310.
- Biermann P. and Steig E. 1996. Estimating rates of denudation using cosmogenic isotope abundances in sediment. *Earth Surface Processes and Landforms* 21:125–139.
- Blakely R. J. 1995. *Potential theory in gravity and magnetic applications*. Cambridge: Cambridge University Press. p. 441.
- Boamah D. and Koeberl C. 2002a. Geochemistry of soils from the Bosumtwi impact structure, Ghana, and relationship to radiometric airborne geophysical data. In *Meteorite impacts in Precambrian shields*, edited by Plado J. and Pesonen L. Impact Studies, vol. 2. Heidelberg: Springer. pp. 211–255.
- Bouchouata A., Canérot J., Souhel A., and Gharib A. 1995. Stratigraphie séquentielle et évolution géodynamique du Jurassique de la région Talmest-Tazoult (Haut Atlas central, Maroc). *Comptes Rendus Hebdomadaires des Séances de l'Académie des Sciences Paris, Série II* 320: 749–756.
- Bougadir B. 1991. Les complexes plutoniques alcalins de la ride de Tassent (Haut Atlas central), Pétrologie, mécanisme et cinématique de mise en place. Ph.D. thesis. Cadi Ayad University of Marrakech-Morocco. 165 p.
- Brechbuhler Y. A. 1983. Etude structurale du Haut Atlas calcaire entre Jbel Ayachi et Rich, Maroc. Ph.D. thesis, Neuchatel University-Switzerland, 128 p.
- Charrière A. and Haddoumi H. 2016. Les “couches rouges” continentales jurassico-crétacées des Atlas marocains (Moyen Atlas, Haut Atlas central et oriental): Bilan stratigraphique, paléogéographiques successives et cadre géodynamique. *Boletín Geológico y Minero* 127(2):407–430.
- Charrière A., Haddoumi H., Mojon P. O., Ferrière J., Cuhe D., and Zili L. 2009. Mise en évidence par ostracodes et charophytes de l'âge paléocène des dépôts discordants sur les rides anticlinales de la région d'Imilchil (Haut Atlas, Maroc): conséquences paléogéographiques et structurales. *Comptes Rendus Pale* 8:9–19.
- Charrière A., Ibouh H., and Haddoumi H. 2011. Le Haut Atlas central de Beni Mellal à Imilchil. In *Nouveaux Guides géologiques et miniers du Maroc 4*, edited by Michard A., Saddiqi O., Chalouan A., Rjimati E. C., and Mouttaqi A. Notes et Mémoires du Service géologique du Maroc 559:109–164.
- Chennaoui Aoudjehane H., Garvie L. A. J., Herd C. D. K., Chen G., and Aboulahris M. 2013. Agoudal: The most recent iron meteorite from Morocco (abstract #5025). *Meteoritics & Planetary Science* 48.
- Chennaoui Aoudjehane H., Reimold W. U., Koeberl C., Bouley S., Aoudjehane M., Aboulahris M., and El Kerni H. 2014. Agoudal (High Atlas Mountains): Confirmation of remnants of a post Mid-Jurassic impact structure in Morocco (abstract #2053). 45th Lunar and Planetary Science Conference. CD-ROM.
- Chennaoui Aoudjehane H., EL Kerni H., Reimold W. U., Baratoux D., Koeberl C., Bouley S., and Aoudjehane M. 2016. The Agoudal (High Atlas Mountains, Morocco) shatter cone conundrum: A recent meteorite fall onto the remnant of an impact site. *Meteoritics & Planetary Science* 51:1497–1518. <https://doi.org/10.1111/maps.12661>.
- Choubert G. and Faure-Muret A. 1962. Evolution du domaine atlasique marocain depuis les temps paléozoïques. Book to the memory of Prof. P. Fallot. Non-standard memory. *Service de la Société Géologique de France* 1:447–514.
- Clark J. F. 1983. Magnetic survey data at meteoritic impact sites in North America. *Geomagnetic Service of Canada, Earth Physics Branch*, Open File 83:1–32.
- Dunlop D. 2002. Theory and application of the Day plot (M_{rs}/M_s versus H_{cr}/H_c). *Journal of Geophysical Research* 107:10. <https://doi.org/10.1029/2001JB000486>.
- El Kerni H., Chennaoui Aoudjehane H., Aboulahris M., Reimold W. U., Koeberl C., Rochette P., Quesnel Y., Uehara M., Hutzler A., Bourles D., Bouley S., and Aoudjehane M. 2014. Agoudal (High Atlas Mountains): Confirmation and first studies of a remnant of a post Mid-Jurassic impact structure (abstract #5318). *Meteoritics & Planetary Science* 49:A109.
- El Moudjahid H., Ibouh H., Bachnou A., and El Harti A. 2016. Mapping and analysis of geological fractures extracted by remote sensing on Landsat TM images, example of the Imilchil-Tounfite area (Central High Atlas, Morocco). *Estudios Geológicos* 72:1–12.
- Ettaki M., Ibouh H., Chellai E. H., and Milhi A. 2007. Les structures « diapiriques » liasiques du Haut-Atlas Central Maroc: Exemple de la ride d'Ikerzi. *Africa Geosciences Review* 14:73–99.

- Fackelman S. P., Morrow J. R., Koeberl C., and McElvain T. H. 2008. Shatter cone and microscopic shock-alteration evidence for a post-paleo-proterozoic terrestrial impact structure near Santa Fe, New Mexico, USA. *Earth and Planetary Science Letters* 270:290–299.
- Fifield L. K., Ophel T. R., Allan G. L., Bird J. R., and Davie R. F. 1990. Accelerator mass spectrometry at the Australian National University's 14 UD accelerator. In *Proceedings of the 5th international conference on accelerator mass spectrometry*, edited by Yiou F. and Raisbeck G. M. *Nuclear Instruments and Methods Research Section B: Beam Interactions with Materials and Atoms* 52:233–237.
- French B. M. and Koeberl C. 2010. The convincing identification of terrestrial meteorite impact structures: What works, what doesn't, and why? *Earth Science Reviews* 98:123–170.
- Frizon de Lamotte D., Zizi M., Missenard Y., Hafid M., El Azzouzi M., Maury R. C., Charrière A., Taki Z., Benammi M., and Michard A. 2008. The Atlas system. In *Continental evolution: The geology of Morocco*, edited by Michard A., Saddiqi O., Chalouan A. and Frizon de Lamotte D. Berlin: Springer. pp. 133–202.
- Froitzheim N., Stets J., and Wurster P. 1988. Aspects of western High Atlas tectonics. *Lecture Notes in Earth Sciences* 15:219–244.
- Fudali R. F. 1979. Gravity investigation of Wolf Creek crater, western Australia. *Journal of Geology* 87:55–67.
- Fudali R. F. and Cressy P. J. 1976. Investigation of a new stony meteorite from Mauretania with some additional data on its find site: Aouelloul crater. *Earth and Planetary Sciences Letters* 81:495–507.
- Hawke P. J. 2004. The geophysical signatures and exploration potential of Australia's meteorite impact structures. Ph.D. thesis, the University of Western Australia-Australia. 314 p.
- Henkel H. 1992. Geophysical aspects of impact craters in eroded shield environments, with special emphasis on electric resistivity. *Tectonophysics* 216:63–90.
- Hutzler A. 2015. Le flux de météorites sur Terre: apport de la mesure de multiples nucléides cosmogéniques, et collectes en milieu désertique. Ph.D. thesis. Aix Marseille University-France. 198 p.
- Hutzler A., Smith T., Rochette P., Bourles D. L., Leya I., and Gattacceca J. 2014. Cosmogenic nuclides study of large iron meteorites (abstract #5243). *Meteoritics & Planetary Science* 49:A179.
- Ibouh H. 1995. Tectonique en décrochement et intrusions magmatiques au Jurassique; tectogenèse polyphasée des rides jurassiques d'Imilchil (Haut Atlas central, Maroc). Ph.D. thesis. Cadi Ayad University of Marrakech-Morocco. 225 p.
- Ibouh H. 2004. Du rift avorté au bassin sur décrochement, contrôles tectonique et sédimentaire pendant le Jurassique (Haut Atlas central, Maroc). Ph.D. thesis, Cadi Ayad University of Marrakech-Morocco. 224 p.
- Ibouh H. and Chafiki D. 2017. La tectonique de l'Atlas: âge et modalités. Le Maroc, paradis des géologues: Société géologue de France 194.
- Ibouh H., Michard A., Charrière A., Benkaddour A., and Rhoujjati A. 2014. Tectonic-karstic origin of the alleged "impact crater" of Lake Isli (Imilchil district, High Atlas, Morocco). *Comptes Rendus Geosciences* 346:82–89.
- Igmoullan B. 1993. Géodynamique méso-cénozoïque de la région de Midelt: Un exemple de l'évolution de la marge septentrionale du bassin du Haut Atlas central (Maroc). Ph.D. thesis. Sémalia University of Marrakesh-Morocco. 181 p.
- Jenny J., Le Marrec A., and Monbaron M. 1981. Les couches rouges du Jurassique moyen du Haut Atlas Central (Maroc) corrélations litho-stratigraphiques, éléments de datation et cadre tectono-sédimentaire. *Bulletin de la Société Géologique de France* 6:627–639.
- Jones A. G., Gough D. I., Kurtz R. D., De Laurier J. M., Boerner D. E., Craven J. A., Ellis R. G., and McNeice G. W. 1992. Electromagnetic images of regional structure in the southern Canadian Cordillera. *Geophysical Research Letters* 19:23–73.
- Kenkmann T., Poelchau M. H., and Wulf G. 2014. Structural geology of impact craters. *Journal of Structural Geology* 62:156–182.
- Kenkmann T., Affi A. M., Stewart S. A., Poelchau M. H., Cook D. J., and Neville A. S. 2015. Saqqar: A 34 km diameter impact structure in Saudi Arabia. *Meteoritics & Planetary Science* 50:1925–1940.
- Kenkmann T., Sturm S., Kruger T., Salameh I., Al-Raggad M., and Konsul K. 2017. The structural inventory of a small complex impact crater: Jebel Waqf as Suwwan, Jordan. *Meteoritics & Planetary Science* 52:351–1370.
- Koeberl C., Milkereit B., Overpeck J. T., Scholz C. A., Amoako P. Y. O., Boamah D., Danuor S., Karp T., Kueck J., Hecky R. E., King J. W., and Peck J. A. 2007. An international and multidisciplinary drilling project into a young complex impact structure: The 2004 ICDP Bosumtwi Crater Drilling Project—An overview. *Meteoritics & Planetary Science* 42:483–511.
- Laville E., Lesage J. L., and Séguret M. 1977. Géométrie, cinématique (dynamique) de la tectonique atlasique sur le versant Sud du Haut Atlas Marocain. Aperçu sur les tectoniques hercyniennes et tardi-hercyniennes. *Bulletin de la Société Géologique de France* 7:499–523.
- Laville E., Zayane R., Honorez J., and Pique A. 1994. Le métamorphisme Jurassique du Haut Atlas Central (Maroc); épisodes syn-schisteux et hydrothermaux. *Comptes Rendus de l'Académie des Sciences de Paris* 318:1349–1356.
- Levine J., Arazi A., Faestermann T., Fernandez Niello J. O., Korschinek G., La Gamma A. M. G., Negri A., Rugel G., Steier P., and Wallner A. 2007. Terrestrial age determination of an achondrite from Rio Cuarto, Argentina (abstract #1362). 38th Lunar and Planetary Science Conference. CD-ROM.
- Lorenz C. A., Ivanova M. A., Artemieva N. A., Sadilenko D. A., Chennaoui Aoudjehane H., Roshina I. A., Korochantsev A. V., and Humayun M. 2015. Formation of a small impact structure discovered within the Agoudal meteorite strewn field, Morocco. *Meteoritics & Planetary Science* 50:112–134.
- McNeill J. D. 1980. Electromagnetic terrain conductivity measurements at low induction numbers. Geonics Limited-Technical Note TN-6.
- Melosh H. J. 1989. *Impact cratering: A geologic process*. New York: Oxford University Press. 245 p.
- Michard A., Ibouh H., and Charrière A. 2011. Syncline-topped anticlinal ridges (STARs) from the High Atlas: a Moroccan conundrum, and inspiring structures from the Syrian Arc, Israel. *Terra Nova*. 23:314–323. <https://doi.org/10.1111/j.1365-3121.2011.01016.x>.

- Milhi A. 1997. *Carte géologique du Maroc, feuille Tinerhir 1/100.000 (Haut Atlas Central). Notes et mémoires du service géologique du Maroc N°377*. Rabat, Morocco: Ministère de l'Énergie et des Mines.
- Montalvo P. E., Cavosie A. J., Kirkland C. L., Evans N. J., McDonald B. J., Talavera C., Erickson T. M., and Lugo-Centeno C. 2018. Detrital shocked zircon provides first radiometric age constraint (<1472 Ma) for the Santa Fe impact structure, New Mexico, USA. *The Geological Society of America Bulletin* 126:720–730.
- Nishiizumi K., Caffee M. W., Lorenz C. A., Ivanova M. A., and Koeberl C. 2017. Cosmogenic radionuclides in Agoudal iron meteorite and associated breccias (abstract #6095). *Meteoritics & Planetary Science* 52:A255. <https://doi.org/10.1111/maps.12943>
- O'Neill C. and Heine C. 2005. Reconstructing the Wolfe Creek meteorite impact: Deep structure of the crater and effects on target rock. *Australian Journal of Earth Sciences* 52:699–709.
- Ormö J., Sturkell E. F. F., Blomqvist G., and Törnberg R. 1999. Mutually constrained geophysical data for the evaluation of a proposed impact structure: Lake Hummeln, Sweden. *Tectonophysics* 311:155–177.
- Pesonen L. J., Bylund G., Torsvik T. H., Elming S. A., and Mertanen S. 1992. Crustal evolution of Fennoscandia-paleomagnetic constraints. *Tectonophysics* 162:27–49.
- Pesonen A., Hadri M., Milhi A., Julien M., and Andrieux J. 1998. The central High Atlas (Morocco). Litho- and chrono-stratigraphic correlations during Jurassic times between Tinjdad and Toufnite. Origin of subsidence. In *Peri-Tethys Mémoire 4: Epicratonic basins of Peri-Tethyan platforms*, edited by Crasquin-Soleau S. and Barrier E. Mémoire du Musée Nationale d'Histoire Naturelle 179:237–256.
- Pesonen L. J., Plado J., Koeberl C., and Elos S. 1998. The Lake Bosumtwi meteorite impact structure, Ghana: Magnetic modeling. *Meteoritics & Planetary Science* 34:91–92.
- Pilkington M. and Grieve R. A. F. 1992. The geophysical signature of terrestrial impact craters. *Reviews of Geophysics* 30:161–181.
- Piqué A., Charroud M., Laville E., and Amrhar M. 2000. The Tethys southern margin in Morocco: Mesozoic and Cenozoic evolution of the Atlas Domain. *Mémoires du Muséum National d'Histoire Naturelle* 182:93–106.
- Plado J., Pesonen L. J., Elo S., Puura V., and Suuroja K. 1996. Geophysical research on the Kärda impact structure, Hiiu Island, Estonia. *Meteoritics & Planetary Science* 31:289–298.
- Poelchau M. H. and Kenkmann T. 2008. Asymmetric signatures in simple craters as an indicator for an oblique impact direction. *Meteoritics & Planetary Science* 43:2059–2072.
- Rahimi A., Bougadir B., Saidi A., Reuber I., and Karson J. A. 1991. Mécanisme de mise en place d'intrusion alcaline en niveau structurale peu profond retracé par les structures d'écoulement magmatique: Exemple du Haut Atlas Central (Maroc). *Comptes Rendus Académique des Sciences de Paris* 313:571–577.
- Ruiz G. M. H., Sebti S., Negro F., Saddiqi O., Frizon de Lamotte D., Stockli D., Foeken J., Stuart F., Barbarand J., and Schaer J. P. 2011. From central Atlantic continental rift to Neogene uplift-western Anti-Atlas, Morocco. *Terra Nova* 23:35–41.
- Ryb U., Matmon A., Erel Y., Haviv I., and Benedetti L. 2014. Styles and rates of long-term denudation in carbonate terrains under Mediterranean to hyper-arid climatic gradient. *Earth and Planetary Science Letters* 406:142–152.
- Sadilenko D. A., Lorenz C. A., Ivanova M. A., Roshchina I. A., and Korochantsev A. V. 2013. A new small impact crater in the High Atlas, in the Agoudal iron strewn field (abstract #5215). *Meteoritics & Planetary Science* 48.
- Salminen R. 2011. Geochemical atlas of Uganda – A new interpretation. Sustainable management of mineral resources project: Geological Mapping, Geochemical Surveys and Mineral Resources Assessment in selected areas of Uganda. Contract No: MEMD/SMMRP/services/2006/000011 IDA. 23 p.
- Schimmelpfennig I., Benedetti L., Finkel R., Pik R., Blard P. H., Bourlès D., Burnard P., and Williams A. 2009. Sources of in-situ ³⁶Cl in basaltic rocks. Implications for calibration of production rates. *Quaternary Geochronology* 4:441–461.
- Schmieder M., Chennaoui Aoudjehane H., Buchner A., and Tohver E. 2015. Meteorite traces on a shatter cone surface from the Agoudal impact site, Morocco. *Geological Magazine* 152: 751–757. <https://doi.org/10.1017/s0016756815000047>.
- Sharma P., Kubik P. W., Fehn U., Gove H. E., Nishiizumi K., and Elmore D. 1990. Development of ³⁶Cl standards for AMS. *Nuclear Instruments Methods in Physics Research Section B: Beam Interactions with Materials and Atoms* 52:410–415. [https://doi.org/10.1016/0168-583X\(90\)90447-3](https://doi.org/10.1016/0168-583X(90)90447-3).
- Souhel A., El Bchari F., Gharib A., El Hariri K., and Bouchouata A. 2000. The Liassic carbonate platform on the western part of the Central High Atlas (Morocco): Stratigraphic and paleogeographic pattern. In *Peri-Tethys Mémoire 5: New data on Peri-Tethyan sedimentary basins*, edited by Crasquin-Soleau S. and Barrier E.. Mémoire du Musée Nationale d'Histoire Naturelle 182:39–56.
- Stöffler D. and Grieve R. A. F. 2007. Metamorphic rocks: A classification and glossary of terms. *Impactites* 2: 82–92.
- Studer M., and du Dresnay R. 1980. Déformations syn-sédimentaires en compression pendant le Lias supérieur et le Dogger au Tizi n'Irhil (Haut Atlas Central de Midelt, Maroc). *Bulletin de la Société géologique de France* 7:391–397.
- Teixell A., Arboleya M. L., Julivert M., and Charroud M. 2003. Tectonic shortening and topography in the central High Atlas (Morocco). *Tectonics* 22:1051–1060.
- Thébault E., Finlay C. C., Alken P., Beggan D. C., Canet E., Chulliat A., Langlais B., Lesur V., Lowes F., Manoj C., Rother M., and Schachtschneider R. 2015. Evaluation of candidate geomagnetic field models for IGRF-12. *Earth, Planets and Space* 67:112–114.
- Tong C. H., Lana C., Marangoni Y. R., and Elis V. R. 2010. Geoelectric evidence for centripetal resurge of impact melt and breccias over central uplift of Araguainha impact structure. *Geology* 38:91–94. <https://doi.org/10.1130/G30459.1>.
- Vasconcelos M. A. R., Leite E. P., and Crósta A. P. 2012. Contributions of gamma-ray spectrometry to terrestrial impact crater studies: The example of Serra da Cangalha, northeastern Brazil. *Geophysical Research Letters* 39:306. <https://doi.org/10.1029/2011GL050525>.

- Warne J. E. 1988. Jurassic carbonate facies of the central and eastern High Atlas rift. Morocco. *Lecture Notes in Earth Sciences* 15:169–199.
- Wright S. and Cavosie A. 2017. Field guide to Santa Fe impact structure. 80th Meteoritical Society Conference. Santa Fe. 23 p.
- Wright S. P., Tegtmeier E. L., and Newsom H. E. 2010. Diversity of breccias associated with the Santa Fe impact structure (abstract #1286). 41st annual Lunar and Planetary Science Conference. CD-ROM.

SUPPORTING INFORMATION

Additional supporting information may be found in the online version of this article:

Material S1. a) Polar plots corresponding to the deviation from concentric strike bedding for eight selected points (point 1: 31°59'12.67"N and 5°30'58.66 W; point 2: 31° 59'18.22"N and 5°30'55.45"W; point 3: 31° 59'16.07"N and 5°30'56.86"W; point 4: 31°59'05.20"N and 5°59.41"W; point 5: 31°59'15.11"N

and 5°30'53.41"W; point 6: 31°59'13.73"N and 5° 30'55.14"W; point 7: 31°59'07.75"N and 5°31'12.2"W; point 8: 31°59'13.60"N and 5°31'07.41"W). The position of the eight selected points, presumed to represent possible centers of the Agoudal impact structure, is presented on the satellite image in Fig. 9a.

Material S2. Map of the analytical signal (AS) over the study area, derived from the RTP magnetic field anomaly map (Fig. 14).
